STARK EFFECT ON THE HYPERFINE STRUCTURE

OF CESIUM^{133}

R. D. HAUN, JR.

TECHNICAL REPORT 322

JANUARY 18, 1957

RESEARCH LABORATORY OF ELECTRONICS

MASSACHUSETTS INSTITUTE OF TECHNOLOGY

CAMBRIDGE, MASSACHUSETTS

MASSACHUSETTS INSTITUTE OF TECHNOLOGY

RESEARCH LABORATORY OF ELECTRONICS

STARK EFFECT ON THE HYPERFINE STRUCTURE
OF CESIUM^{133}

R. D. Haun, Jr.

Abstract

The change of the hyperfine-structure separation energy caused by an electric field
has been measured in cesium^{133} by the atomic-beam magnetic-resonance method. The
shift of the $(F = 4, \; m_F = 0) \longleftrightarrow (F = 3, \; m_F = 0)$ transition frequency (9192.6 mc/sec)
caused by electric field $\mathscr{E}$ is given by $\Delta(\mathscr{E}) = -2.29 \times 10^{-6} (1 \pm .03) \mathscr{E}^2$ cps, where
$\mathscr{E}$ is in volt/centimeter. This number is 2.8 times the value predicted from the atomic
polarizability measurements of H. Scheffers and J. Stark, if a simplified theory that
neglects hyperfine-structure perturbations of the ground-state wave functions is used.
A more precise theory which takes into account these wave-function differences has
been outlined but the calculations have not been carried out in detail.

Table of Contents

iii

I. INTRODUCTION

In recent years the main goal of the atomic beam laboratory of the Research Laboratory of Electronics, M.I.T., has been the development of high-precision frequency-measurement techniques. These techniques have already found practical application in industry with the manufacture of a cesium atomic-beam frequency standard that uses the high-Q resonance properties of the cesium atom to provide a stable, known frequency. The feasibility of such a device was investigated by Zacharias, Yates, and Haun (34, 35). During this study it was suggested that the high-precision frequency-measurement techniques that were then under development might be used to investigate the effect of a strong homogeneous electric field on atomic hyperfine-structure energy levels. Since this effect had not previously been studied, it was felt that the problem would be of interest as a test of our present understanding of atomic theory. This report describes a study of these electric polarization effects on the hyperfine structure of cesium[133].

In this experiment the change in the ground-state hyperfine-structure energy separation is measured as a function of applied electric field. This is done by comparing the $(F=4, m_F=0) \leftrightarrow (F=3, m_F=0)$ energy separation without electric field with the same energy separation with electric field. An early theory (24) for the electric polarization effect on hyperfine structure implied that a fairly direct comparison could be made with the value of the atomic polarizability of cesium obtained in electrostatic deflection experiments by Scheffers and Stark (25). The measurements described in this report give values for the polarizability that are 2.8 times larger than the value of Scheffers and Stark if this theory is used. Schwartz (26) has recently suggested a more sophisticated theory that may remove this discrepancy.

Several innovations in atomic-beam technique which have been made in this experiment will be described in detail. In summary, they are:

1. The use of a crystal-stabilized klystron as the exciting source for producing the transitions.

2. The use of a technique in which the atomic system is perturbed in a region between the two radiofrequency transition regions.

3. The use of an apparatus geometry in which the source and detector are offset to opposite sides of the axis of the apparatus. This geometry yields resonance lines with reduced linewidths and no loss in signal-to-noise, as compared with conventional geometry.

4. The use of well-collimated atomic-beam sources.

5. The use of an automatic data-recording system in which frequency differences and resonance curves are presented visually as a permanent record.

The last three of these innovations were first used on the feasibility study test model. These techniques will be discussed here, since a detailed discussion has not yet appeared.

II. THEORY

2.1 HYPERFINE STRUCTURE

A brief review of the theory of atomic hyperfine structure will be presented. A more complete and sophisticated treatment can be found in the work of Schwartz (27) and Ramsey (19).

Atomic hyperfine structure arises from the interaction of the distributed nuclear electric charge and magnetism with the electron cloud that surrounds the nucleus. If an expansion of the charge and magnetism distributions is performed in terms of multipoles, the hyperfine-structure perturbation can be written as

$$H' = aI \cdot J + bQ_{op} + cO_{op} + \ldots$$

where $aI \cdot J$ is the term that describes the interaction between the nuclear magnetic dipole moment and the electron cloud, bQ_{op} describes the interaction of the nuclear electric quadripole moment with the electrons, and cO_{op} describes the interaction of the nuclear magnetic octopole moment with the electrons (27). [Odd-n electric, and even-n magnetic, 2^n-pole moments are zero for systems of definite parity (20).]

For cesium^{133} in the ground state, the total electronic angular momentum J is 1/2, and the nuclear angular momentum I is 7/2. Therefore, with no external field the vector sum rule gives two hyperfine-structure energy levels: $F(\equiv \vec{I} + \vec{J}) = 4$ and $F = 3$. The energy difference $h\Delta\nu$ between these two levels corresponds to $9,192,631,830 \pm 10$ cps (9). Since J is less than one, all moments higher than the magnetic dipole moment will produce no effect on the ground-state hyperfine structure (20).

When an atom is placed in a magnetic field B each of the hyperfine-structure energy levels splits into $2F + 1$ sublevels, because of the interaction

$$H'' = \frac{\mu_J}{J} J \cdot B + \frac{\mu_I}{I} I \cdot B$$

For atoms with total angular momentum $J = 1/2$, the magnetic dependence of the hyperfine-structure sublevels is given by the Breit-Rabi formula (2) as

$$W(F, m_F) = -\frac{\Delta W}{2(2I + 1)} - \frac{\mu_I}{I} Bm_F \pm \frac{\Delta W}{2} \left(1 + \frac{4m_F}{2I + 1} x + x^2\right)^{1/2}$$

where

$$x = \frac{\left(-\frac{\mu_J}{J} + \frac{\mu_I}{I}\right) B}{\Delta W}$$

and ΔW is the zero-field separation between the two hyperfine-structure energy levels ($= h\Delta\nu$). The plus sign applies for $F = I + \frac{1}{2}$; the minus sign is used when $F = I - \frac{1}{2}$. This magnetic-field dependence is plotted in Fig. 1 for the special case $I = 7/2$, which

2
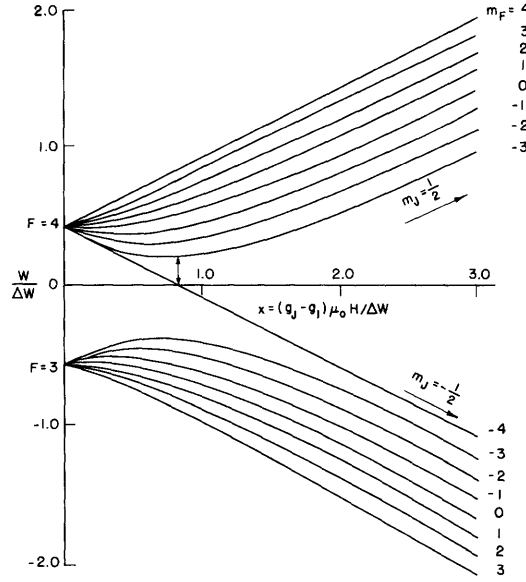
Fig. 1. Magnetic dependence of hyperfine-structure
energy levels for J = 1/2, I = 7/2.

is the case for cesium[133].

The most important facts concerning the magnetic-field dependence of the cesium[133]
hyperfine structure (as far as the electric polarization-effect experiment is concerned)
are:

1. At high magnetic fields the slopes of the two levels (F=4, m_F=0) and (F=3, m_F=0)
are equal and opposite.

2. In weak magnetic fields the difference in energy between the (4, 0) and the (3, 0)
levels is given by (4, 0 ←→ 3, 0) = $\Delta\nu$ + 427B^2 cps, where $\Delta\nu$ is the zero-field hyperfine-
structure separation and B is the magnetic field in gauss.

2.2 ELECTRIC POLARIZATION EFFECTS ON ATOMIC HYPERFINE STRUCTURE

Before discussing the high-precision techniques used in this experiment, we shall
briefly speak of the theory of the electric effects on hyperfine structure, in order to
see why high precision of this order is necessary.

The Hamiltonian H for an atom in combined electric and magnetic fields can be
written as

$$H = H_o + H_{hfs} + er \cdot \mathscr{E} + \mu \cdot B \qquad (1)$$

where H_o is the Hamiltonian describing the coulomb interaction between the nucleus and
the electrons and between electrons and electrons, and the fine-structure interaction
between the intrinsic and orbital moments of the electrons; H_{hfs} is the term describing
the interaction of the nuclear moments with the field of the electrons; e is the electronic
charge; r is the radius vector; $\mathscr{E}$ is the electric field; μ is the total atomic magnetic

3

moment; and B is the external magnetic field.

In the ground state of cesium^{133} the H_{hfs} term is of the order of 10^{10} cps. As we shall see, $er \cdot \mathscr{E}$ is of the order of 10^{7} to 10^{8} cps for the values of electric field used in this experiment, and $\mu \cdot B$ is of the order of 200 cps-gauss^{2} for the $m_F=0$ levels. Therefore each term in Eq. 1 is small in comparison with the preceding terms so that perturbation theory can be applied to each term separately.

The following order-of-magnitude calculation was suggested by C. H. Schwartz (24):

Since we can choose the coordinate axes so that $er \cdot \mathscr{E} = ez\mathscr{E}$, which has odd parity, and since the atomic ground state has well-defined parity, the diagonal matrix elements of the electric-field perturbation are zero.

Proceeding to second order, we obtain a nonzero energy shift:

For the F=4 level
$$\Delta_4 = \sum_n \frac{|<n, L=1|ez\mathscr{E}|n=6, L=0>|^2}{W^O(n=6, L=0, F=4) - W^O(n, L=1)}$$

For the F=3 level
$$\Delta_3 = \sum_n \frac{|<n, L=1|ez\mathscr{E}|n=6, L=0>|^2}{W^O(n=6, L=0, F=3) - W^O(n, L=1)}$$

But $W^O(n=6, L=0, F=3) + h\Delta\nu = W^O(n=6, L=0, F=4)$ where $\Delta\nu$ is the hyperfine-structure separation previously defined. Therefore we can rewrite Δ_4 as

$$\Delta_4 \doteq \sum_n \frac{|<n, L=1|ez\mathscr{E}|n=6, L=0>|^2}{W^O(n=6, L=0, F=3) - W^O(n, L=1)} \left(1 + \frac{h\Delta\nu}{W^O(n, L=1) - W^O(n=6, L=0)}\right)$$

So that, if we consider only perturbations to the 6p state of cesium, and neglect the fact that the wave function for the F=4 level is slightly different from the wave function for the F=3 level, the shift of the hyperfine-structure separation $\Delta\nu$ caused by the electric field is

$$\Delta(\mathscr{E}) = \Delta_4 - \Delta_3 = -\frac{h\Delta\nu}{(W^O(n=6, L=1) - W^O(n=6, L=0))} \frac{|<n=6, L=1|ez\mathscr{E}|n=6, L=0>|^2}{(W^O(n=6, L=1) - W^O(n=6, L=0))}$$

The energy E of an atom of polarizability α in an electric field $\mathscr{E}$ is given by $E = \frac{1}{2}\alpha\mathscr{E}^2$. But this is just the second-order perturbation energy of the ground-state level, which, for cesium, can be written (30)

$$E \doteq -\frac{|<n=6, L=1|ez\mathscr{E}|n=6, L=0>|^2}{W^O(n=6, L=1) - W^O(n=6, L=0)}$$

Scheffers and Stark (25) measured α by electrostatic deflection of a beam of cesium atoms. The value they obtained was $\alpha = (42. \pm 2.) \times 10^{-24}$ cm^3. We therefore obtain

$$\Delta(\mathscr{E}) = -\frac{1}{2}\alpha\mathscr{E}^2 \frac{h\Delta\nu}{W^O(n=6, L=1) - W^O(n=6, L=0)}$$

$$= -0.82 \times 10^{-6}\mathscr{E}^2 \text{ cps}$$

4

where $\mathscr{E}$ is in volts per centimeter.

For $\mathscr{E} = 10^5$ volts/cm (a reasonably high value) we see that the shift in the hyperfine-structure separation frequency caused by the electric field should only be approximately 8×10^3 cps. Since the hyperfine-structure separation is 9192 mc, the necessity for a high-precision experiment is obvious. The actual experimental results give a hyperfine-structure shift that is approximately 2.8 times larger than that predicted by this theory.

Schwartz (26) has recently suggested that this theory is incorrect because it fails to take into account the fact that the wave functions for the F=4 and the F=3 levels differ in amounts of the order $\dfrac{h\Delta\nu}{W_{6p}^{(o)} - W_{6s}^{(o)}}$. A more sophisticated theory that takes into account this difference is outlined in Appendix I.

2.3 ATOMIC-BEAM MAGNETIC-RESONANCE METHOD

The molecular-beam magnetic-resonance method was first used by Rabi (21). Since this method has been fully described (19, 28, 11) only a brief review will be presented here.

An atomic-beam apparatus consists of an evacuated enclosure in which a source of atoms and a device for detecting these atoms are placed. In the magnetic-resonance method an atom moving from the source to the detector passes through two inhomogeneous magnetic fields. Since the slope of the energy-as-a-function-of-magnetic-field curve is the negative of the effective magnetic moment, the atoms will be deflected by these inhomogeneous magnets in different ways, depending upon which of the energy levels the atom occupies as it moves through the field. By subjecting the atom to a weak oscillating magnetic field of a frequency corresponding to the energy difference between two states, the atom can be made to undergo a transition ("flop") from one state to another. In the atomic-beam magnetic-resonance method these transitions take place in the space between the two inhomogeneous fields so that the state of the atom, and hence its deflection, in the second inhomogeneous field is a function of the frequency of the applied oscillating field. Therefore, for a given detector position, the number of detected atoms is a function of the frequency of the oscillating field.

In the "flop-in" technique (36), which was used in this experiment, the inhomogeneous magnetic fields are arranged so that the deflections in the two magnets add if the applied frequency does not induce transitions between two states with opposite signs of magnetic moment in the two deflecting magnets, whereas the deflections cancel if the atom does undergo a transition that reverses the sign of its magnetic moment in the second magnet relative to the first. The detector is placed so that it intercepts only those atoms that undergo such transitions.

In the apparatus described in this report the magnetic fields in the deflecting magnets are large (approximately eight kilogauss) and the magnetic field in the transition region is small (approximately one-half gauss).

Since the natural lifetime of the energy levels involved in atomic-beam experiments

5

is usually very long, the width of the resonance curve obtained by using the atomic-beam magnetic-resonance technique is determined by the amount of time the atom spends in the transition region. This can be thought of as a consequence of the Heisenberg uncertainty principle. There are, therefore, two ways to obtain narrow resonances in an atomic-beam apparatus: One is to make the transition region long; the other is to make the velocity of the atoms small as they move through the transition region. Both of these steps have been taken to some degree in the apparatus described here: The transition region is approximately 80 cm long, and an offset geometry was used. The use of offset geometry lowers the mean velocity of the beam atoms by a factor of approximately two from the value which would be obtained with conventional geometry. The calculations for this offset geometry are outlined in Appendix II.

2.4 RAMSEY TWO-TRANSITION-REGION METHOD

a. General Discussion

As we have mentioned, one of the ways to obtain narrow resonance curves is to make the transition region long. However, if the oscillating field is applied over a long region, standing waves will be present and the motion of the beam will cause a broadening of the resonance curve on account of the Doppler shift. This broadening can be reduced by using a cavity very near cutoff as the transition region because then only one half standing wave will be present in the cavity. Ramsey (22) has suggested a two-transition-region method which eliminates Doppler broadening and gives a linewidth that is one-half that given by a single transition region — even if Doppler broadening is eliminated. This method has the further advantage that it yields resonances that correspond to the average energy of the atom in the transition region.

In the Ramsey method the atom passes through a radiofrequency field in a time τ, then drifts through an rf-free region for a time T, and finally is acted upon by another rf field for time τ.

The following classical analogy (22) is helpful in understanding this method: Consider a classical system with angular momentum $\vec{L}$ and associated magnetic moment $\vec{\mu}$. Let the angular precession frequency of this system be ω_O in the two rf regions and $\bar{\omega}_O$ in the intermediate region. Assume that $\vec{\mu}$ is parallel to the constant magnetic field $\vec{B}_O$ in the transition region as it enters the first rf field. If the frequency ω of the applied rf field is approximately equal to ω_O, then the rotating magnetic field $\vec{B}_{rf}$ will tend to increase the angle ϕ between $\vec{\mu}$ and $\vec{B}_O$. By suitably choosing B_{rf} and τ we can make the change in angle ϕ 90° in the first rf region.

If $\bar{\omega}_O = \omega_O$, and the phases and amplitudes of the rf fields are the same, then the magnetic-moment vector $\vec{\mu}$ will enter the second rf region in phase with $\vec{B}_{rf}$ and ϕ will increase to 180° as the system moves through this region. The sign of the magnetic moment with respect to $\vec{B}_O$ is reversed which corresponds to a quantum-mechanical transition between two states separated by an energy $\hbar\omega_O$.

If $\bar{\omega}_O \neq \omega_O$, the magnetic-moment vector $\vec{\mu}$ will lag behind the rf magnetic vector

$\tilde{B}_{rf}$ by $(\omega - \bar{\omega}_0)T$ as it enters the second region. These two vectors will be in phase if $\omega = \bar{\omega}_0$, so that the maximum of the resonance peak will occur when $\omega = \bar{\omega}_0$. (In this argument we have used the fact that the pulse of radiation with frequency ω and duration τ can be Fourier-analyzed into a continuous spread of frequencies about the center frequency ω.) Therefore, we see that the Ramsey method gives resonances that correspond to the average precession frequency of the system in the drift region between the two rf regions. The quantum-mechanical analogy is a transition between two states separated by $\hbar\bar{\omega}_0$, the average energy difference in the drift region.

This property of the Ramsey method has been utilized in the experiment described in this report: The electric field which is used to perturb the hyperfine-structure energy levels is applied only in the region between the two rf cavities.

A more rigorous treatment of the case $\bar{\omega}_0 \neq \omega_0$ is given below. It will be found there that the statement that the maximum of the Ramsey resonance pattern occurs when $\omega = \bar{\omega}_0$ is only approximately true. The apparent resonant frequency is actually shifted from the value $\bar{\omega}_0$ by amounts that are of the order of $(\omega_0 - \bar{\omega}_0)\frac{\tau}{T}$.

This argument was somewhat simplified by assuming that all of the systems move through the transition region in the same time. In actual application the velocity distribution of the atomic beam will give rise to a spread of these transit times. This results in cancellation of the subsidiary Ramsey peaks which occur whenever $(\omega - \bar{\omega}_0)T = n \cdot 2\pi$, where n is an integer. This cancellation of side peaks is a phenomenon similar to that observed in white-light fringes. The wider the velocity distribution, the better will be the cancellation of the side peaks. Our apparatus was designed so as to have a wide velocity spread (see Appendix II).

b. Asymmetries in the Line Shape Caused by Differences in Energy
   at and between the Transition Regions

1. General Discussion

We shall now present a rigorous quantum-mechanical description applied to atoms whose energy levels in the two transition regions differ from the levels in the drift region.

Let us consider a beam of atoms with velocity v that moves through a two-cavity rf system that consists of two cavities of length ℓ in which there is an rf field of frequency ω, separated by a drift region of length L. Assume that the atoms have two energy levels, W_p and W_q in the rf regions, and that these levels have different energy values $\overline{W}_p$ and $\overline{W}_q$ in the drift region. Let $\hbar\omega_0 = W_p - W_q$ and $\hbar\bar{\omega}_0 = \overline{W}_p - \overline{W}_q$. Assume that the radiofrequency field can be resolved into two circularly polarized waves, each of which gives rise to a perturbation of the form $V_{pq} = -V_{pq} = \hbar b\, e^{-i\omega t}$ where b is proportional to B_{rf}/B_0. B_{rf} is the magnitude of the magnetic vector for the circularly polarized wave that produces the perturbation, and B_0 is the magnitude of the static magnetic field in the rf cavities. [This will be the form of the perturbation for an atom in an oscillating magnetic field (19).]

7

Ramsey (22) derives the following expression for the transition probability for changes from state p to state q as the atom moves through the entire rf system:

$$P_{pq} = 4 \left(\frac{2b}{a}\right)^2 \sin^2 \frac{1}{2} a\tau \left(\cos \frac{1}{2}\lambda T \cos \frac{1}{2} a\tau - \frac{\omega_0 - \omega}{a} \sin \frac{1}{2}\lambda T \sin \frac{1}{2} a\tau\right)^2$$

where $a = \left[(\omega_0 - \omega)^2 + (2b)^2\right]^{1/2}$, $\lambda = \bar{\omega}_0 - \omega$, $b = \frac{1}{2} g\mu_0 B_{rf}$, $\tau = \ell/v$, and $T = L/v$.

Letting $\overline{\Delta(\mathscr{E})} = (\omega_0 - \bar{\omega}_0)$ and $\delta = (\omega - \bar{\omega}_0)$, we can rewrite this expression as

$$P_{pq} = 4 \frac{(2b)^2}{(\overline{\Delta(\mathscr{E})} - \delta)^2 + (2b)^2} \sin^2 \frac{1}{2} a\tau \left(\cos \frac{\delta}{2} T \cos \frac{a}{2}\tau + \frac{\overline{\Delta(\mathscr{E})} - \delta}{a} \sin \frac{\delta}{2} T \sin \frac{a}{2}\tau\right)^2$$

Now we note that the terms involving T are the most rapidly varying functions of the applied frequency, and thus they determine the gross features of the Ramsey resonance pattern. We see immediately that for $\overline{\Delta(\mathscr{E})} = 0$ the maximum of P_{pq} occurs for $\delta = 0$. We want to determine how great an error is involved in assuming that the maximum of P_{pq} occurs for $\delta = 0$ in the more general case when $\overline{\Delta(\mathscr{E})}$ is not zero.

Let us assume that this error is small so that we need only consider a small range of δ about zero, i.e., let us consider only $\delta \ll \overline{\Delta(\mathscr{E})}$. With this assumption we can write

$$a \doteq \sqrt{(\overline{\Delta(\mathscr{E})})^2 + (2b)^2}$$

and

$$P_{pq} \doteq 4 \left(\frac{2b}{a}\right)^2 \sin^2 \frac{a}{2}\tau \left(\cos \frac{\delta}{2} T \cos \frac{a}{2}\tau + \frac{\overline{\Delta(\mathscr{E})}}{a} \sin \frac{\delta}{2} T \sin \frac{a}{2}\tau\right)^2 \tag{2}$$

in which only the terms that contain δ explicitly are dependent on the applied frequency ω.

2. Special Case: Limit of Zero Power

Differentiating P_{pq} with respect to δ and setting the result equal to zero, we obtain the condition for maxima as

$$\tan \frac{1}{2} \delta_E T = \frac{\overline{\Delta(\mathscr{E})}}{a} \tan \frac{1}{2} a\tau$$

for $(2b)^2 \ll (\overline{\Delta(\mathscr{E})})^2$, this reduces to

$$\tan \frac{1}{2} \delta_E T = \tan \frac{1}{2} a\tau$$

i.e.,

$$\delta_E = \overline{\Delta(\mathscr{E})} \frac{\tau}{T}$$

This is the error involved in the assumption that the maximum of the central Ramsey

resonance peak occurs at the frequency corresponding to the mean-energy difference for the atom in the drift region (i.e., for $\omega = \bar{\omega}_o$) if the rf power is small.

3. General Case of Nonzero Power

When the rf power is adjusted for maximum Ramsey flop amplitude, the term $(2b)^2$ is not negligible in comparison with $\overline{(\Delta(\mathscr{E}))^2}$. We must therefore take into account the velocity distribution of the atoms that reach the detector of the apparatus. To perform this calculation, we use Eq. 2 in its full form.

In Eq. 2 we note that, since a is a function of the rf power, the magnitude of the second term in the brackets is a function of the rf power. But it is just this term that gives rise to the error. Therefore we expect the observed resonant frequency to have some dependence on rf power. Let us examine this dependence.

Let $\left(\dfrac{dN}{d\left(\frac{v}{\alpha}\right)}\right) d\left(\dfrac{v}{\alpha}\right)$ be the relative number of flopped atoms that have velocities in the range v to v + dv. (By "flopped atoms" we mean atoms that have undergone transitions between states p and q.) The transition probability averaged over the velocity distribution is then given by

$$\overline{P_{pq}} = \int_0^\infty \frac{dN}{dy} \left(P_{pq}(y)\right) dy$$

Using Eq. 2 for P_{pq} and applying some trigonometrical identities, for the transition probability averaged over the velocity distribution, we can write

$$\overline{P_{pq}} = \frac{1}{1-\rho^2} \left[\left(\frac{1}{4} + \frac{3}{4}\cos\theta\right) I(0) + \left(\frac{1}{4} - \frac{3}{4}\cos\theta\right) I(2\gamma) \right.$$

$$+ (-\cos^2\theta)\, I(2\beta) + \left(-\frac{1}{4} + \frac{1}{4}\cos^2\theta\right) I(4\beta)$$

$$+ \frac{1}{2}\cos\theta\,(1 + \cos\theta)\, I(2\beta - 2\gamma)$$

$$+ \frac{1}{2}\cos\theta\,(-1 + \cos\theta)\, I(2\beta + 2\gamma)$$

$$+ \left[-\frac{1}{8} - \frac{1}{4}\cos\theta\left(1 + \frac{1}{2}\cos\theta\right)\right] I(4\beta - 2\gamma)$$

$$\left. + \left[-\frac{1}{8} + \frac{1}{4}\cos\theta\left(1 + \frac{1}{2}\cos\theta\right)\right] I(4\beta + 2\gamma) \right]$$

where

$$I(m) = \int_0^\infty \frac{dN}{dy} \cos\frac{m}{y}\, dy,$$

9

$$\cos\theta = \frac{\overline{\Delta(\mathscr{E})}}{a} = \frac{\rho}{\left(1+\rho^2\right)^{1/2}},$$

$$\rho = \frac{\overline{\Delta(\mathscr{E})}}{2b},$$

$$\beta = \frac{a\ell}{2a} = \frac{b_o\ell}{a}\frac{b}{b_o}\left[1+\left(\rho_o\frac{b_o}{b}\right)^2\right]^{1/2},$$

$$\rho_o = \frac{\overline{\Delta(\mathscr{E})}}{2b_o},$$

$$\gamma = \frac{\delta L}{2a} = \delta\,\frac{\ell}{2a}\frac{L}{\ell},$$

and $b_o\dfrac{\ell}{a} = 0.3\pi$, b_o being the value of b that makes the amplitude of the Ramsey reso-nance maximum for the $v^3\exp\left[-\left(\frac{v}{a}\right)^2\right]$ velocity distribution.

This function was plotted for each of five values of b/b_o at each of five values of $\overline{\Delta(\mathscr{E})}/2b_o$. The error that resulted from the assumption that the maximum of the central Ramsey resonance peak occurs at $\omega = \omega_o$ was determined directly from each plot. The error frequency δ_E obtained in this way is plotted in Figs. 2 and 3 as a function of b/b_o and $\overline{\Delta(\mathscr{E})}/2b_o$. (The error frequency $\delta_E = (2\gamma_E a)/L$ is plotted in units of $2a/L$ on these graphs on the following page.) These calculations were performed by the Joint Computation Group of the Research Laboratory of Electronics, M.I.T., and are on file there.

The two plots correspond to two different assumed velocity distributions (see Appendix II):

1. In Fig. 2 the $v^3\exp\left[-(v/a)^2\right]$ distribution was used.

2. In Fig. 3 the assumed distribution was

$$\frac{dN}{d\left(\frac{v}{a}\right)} = \begin{cases} 0 & \text{for} & 0.6 > v/a > 2.3 \\[2mm] 3.25\frac{v}{a} - 1.95 & \text{for} & 0.6 \leq v/a \leq 1.0 \\[2mm] 2.30 - \frac{v}{a} & \text{for} & 1.0 \leq v/a \leq 2.3 \end{cases}$$

There is an advantage in using the $v^3\exp\left[-(v/a)^2\right]$ distribution, since accurate tables of the integral I(m) are available (19, 14). A table of the function I(m) was calculated for the other distribution and it is also on file. The accuracy of this table is approximately one per cent, but this was sufficient for the calculations made for this report.
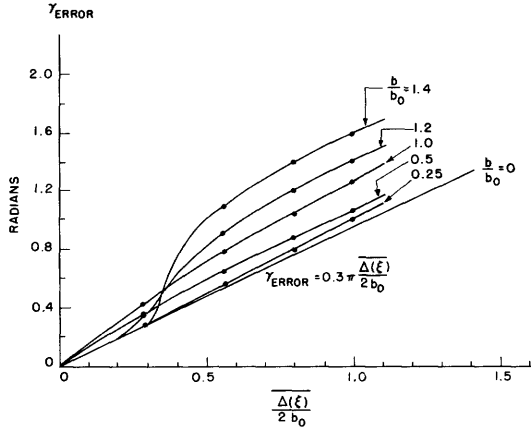
γ_{ERROR}

RADIANS

2.0

1.6

1.2

0.8

0.4

0

$\frac{b}{b_o} = 1.4$
1.2
1.0
0.5
0.25
$\frac{b}{b_o} = 0$

$\gamma_{ERROR} = 0.3\pi \frac{\overline{\Delta(\xi)}}{2b_o}$

0   0.5   1.0   1.5

$\frac{\overline{\Delta(\xi)}}{2b_o}$

Fig. 2.   Asymmetry correction
$v^3 \exp(-V/a)^2$.

γ_{ERROR}

RADIANS

2.0

1.6

1.2

0.8

0.4

0

$\frac{b}{b_o} = 1.4$
1.2
1.0
0.5
0.25
$\frac{b}{b_o} = 1.6$
$\frac{b}{b_o} = 0$

$\gamma_{ERROR} = 0.3\pi \frac{\overline{\Delta(\xi)}}{2b_o}$

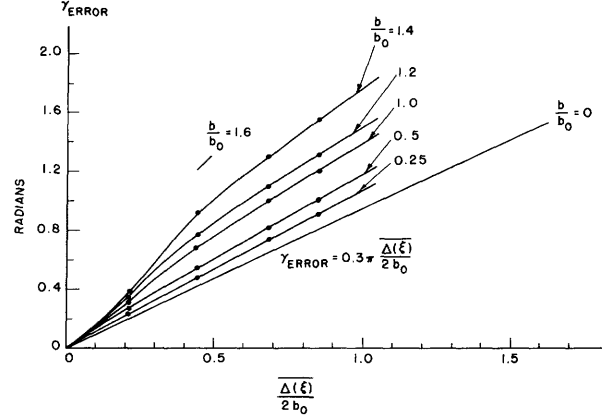0   0.5   1.0   1.5

$\frac{\overline{\Delta(\xi)}}{2b_o}$

Fig. 3.   Asymmetry correction
(derived distribution).

The correction-frequency graphs have been plotted using the dimensionless parameter $\gamma = (\delta L)/2a$, b/b_o, and $\overline{\Delta(\mathcal{E})}/2b_o$ so that they can be applied to any other experiment in which the velocity distribution approximates one of the two assumed velocity distributions — regardless of the mean velocity, the dimensions of the rf system, or the reason for the energy difference $\hbar \overline{\Delta(\mathcal{E})}$. In order to apply the charts to other problems, we merely find the value of a that makes the velocity scale of the assumed velocity distribution fit the distribution for the given problem. With this value of a we then compute the values of b_o and δ/γ from the aforementioned definitions. The error frequency for a given difference $\overline{\Delta(\mathcal{E})} = \omega_o - \bar{\omega}_o$ can then be obtained from the graph.

Note that for both velocity distributions the asymmetry correction can be broken into two parts.

1. A velocity-independent correction which is given by $\delta_E = \overline{\Delta(\mathcal{E})} (\ell/L)$. This is just the correction for $b = 0$ that was previously discussed.

2. A correction that depends on the rf power $(b/b_o)^2$, and therefore on the velocity distribution. This part of the correction is the difference between the total correction and the correction for $b = 0$.

For optimum rf power $(b/b_o = 1)$ these parts of the asymmetry correction are of comparable magnitude.

11

III. EXPERIMENTAL APPARATUS

3.1 GENERAL DESCRIPTION

Preliminary measurements of the Stark effect on cesium[133] by hyperfine structure were carried out on the feasibility study test model of the atomic-beam frequency standard. However, that apparatus was not entirely satisfactory because of the excessive length of the deflecting magnets and the smallness of the apertures through which the atomic beam was forced to pass, and because of vacuum difficulties which were attributed to a reduced pumping speed caused by the use of large amounts of tubing of small diameter and by the use of one small diffusion pump for the entire system.

Since we felt that this feasibility test model would not be suitable as a laboratory frequency standard for regular use, a new apparatus was constructed and used for the experiment described in this report.

In analyzing the performance of the earlier apparatus it was pointed out that the observed field-dependent transition frequency is dependent on the relative phase of the rf fields in the two Ramsey transition regions. Holloway (11) has studied this source of error in detail. His results can be summarized by stating that, for a small phase difference δ (radians), the error E (in cps) in the observed peak frequency is given by $E = \frac{\delta}{\pi}$ (halfwidth of central Ramsey peak). In order to eliminate this source of error, the new apparatus was designed so that two beams could be operated simultaneously. These beams move in opposite directions through the Ramsey transition regions, so that a phase difference that appears as a lag to one beam appears as a lead to the other beam.

For the Stark-effect measurement, one of the two beams was provided with a pair of parallel condenser plates in the transition-region drift space, the other beam was electrostatically shielded from this field. The peak transition frequencies for the two beams were to be measured and compared as a function of the applied electric field.

However, some difficulty was encountered in operating both beams simultaneously because of the large background at each detector from the source of the other beam. Consequently an alternative scheme which used only one beam was employed for the measurements described here. Since this method proved sufficient for the experiment, no further attempts were made to observe both beams at the same time — although baffles were installed between the sources and the detectors which, it is hoped, will reduce the background to a usable level when the apparatus is put into operation as a frequency standard.

The various components used in the experiment will now be discussed.

3.2 THE BEAM TUBE

A simplified diagram of the arrangement of the components that are inside the vacuum is shown in Fig. 4. Only one beam is shown in this figure; the source and detector positions are interchanged for the other beam. It is interesting to remark

12

Fig. 4. Arrangement of apparatus.

that atoms that undergo transitions in the beam shown in Fig. 4 experience stimulated absorption, while atoms in the other beam experience stimulated emission. The reason for the use of offset geometry (i.e., a geometry in which the source and detector are on opposite sides of the center line of the apparatus) are outlined in Appendix II in which the velocity distribution for the "flopped" beam is derived.

The source, deflecting magnets, transition cavities, detector, and other auxiliary components are described in Appendix IV. The components that are of direct interest in the interpretation of the electric polarization effect experiment are described in this section.

a. Stark-Field Electrodes

The Stark field is obtained with a parallel-plate condenser in the drift region between the high-frequency transition cavities (see Figs. 4 and 29). The cross section of the Stark electrodes is shown in Fig. 5. One of the two atomic beams in the apparatus is shielded from the electric field applied to the other by a cylindrical electrostatic shield. Each Stark electrode is a piece of brass 26 inches long, one face of which is milled flat within 0.001 inch. The edges of the electrodes were rounded because the clearance between the plates and the surrounding grounded surfaces of necessity is very small at some points. Each of the electrodes is supported by four Teflon insulators. Although the Teflon is subjected to both compression and shear stresses, no change in the gap width has been observed over a period of six months. The gap between the two flat surfaces was adjusted to be 0.250 ± 0.002 inch with a gauge block during the assembly of the apparatus and was checked periodically with an inside micrometer.

Before machining the electrodes we examined the homogeneity of the field that they produce by testing a model in an electrolytic tank. By cutting off the beam so that it cannot move in the region which is less than 3/16 inch from the edge of the electrodes, the variation of the average squared field applied to the beam is made less than 1 per cent. This estimate of the homogeneity is verified by the observation that the central Ramsey flop peak does not increase in width when the Stark voltage is increased. (See section 5.3.)
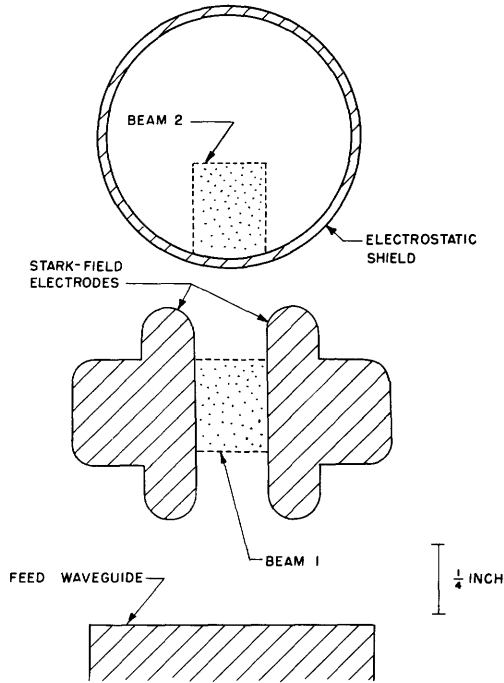
13

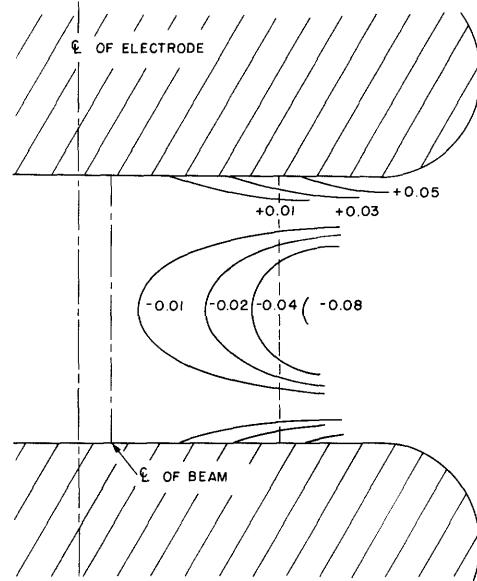Fig. 5. Cross section of Stark-field electrodes.

Fig. 6. Stark-field homogeneity. The beam moves perpendicularly to the plane of figure.

The effective length (see section 5.6a) of the Stark-field region is defined by the relation

$$\left(\frac{V}{d}\right)^2 \cdot L_{eff} = \int_{-\infty}^{\infty} \mathscr{E}^2 \, dx$$

where V is the voltage difference between the electrodes, d is the distance between the two flat surfaces, L_{eff} is the effective length, $\mathscr{E}$ is the electric field at the point x, and x is distance measured along the length of the atomic beam. The integral can be approximated by taking note of the fact that the electrodes are approximately equivalent to the equipotentials, $\frac{3}{22} \cdot d$ and $\frac{19}{22} \cdot d$, from one of a pair of infinitesimally thin electrodes with separation $s = \frac{11}{8} \cdot d$. We can then use the analytical form given by Morse and Feshbach (15) for the stray field $\mathscr{E}$ at the ends of the electrodes. Proceeding in this way, we obtain

$$L_{eff} = 66.0 + 0.1 \pm 0.05 \text{ cm}$$

where the indicated error is the estimated maximum error in the approximation. This value of L_{eff} holds for all paths through the space between the Stark electrodes (on or off the center line). We therefore conclude that the error made by using the geometrical length (66.0 cm) of the Stark electrodes as the effective length of the effective field

is less than 0.2 per cent.

We can also use this approximation to obtain another estimate of the homogeneity of the square of the electric field at different points in the cross section of the beam. In Fig. 6 the values of $\left(\dfrac{\mathscr{E}^2}{(V/d)^2} - 1\right)$ for this approximation are plotted as a function of position. The boundaries of half of the beam cross section are shown in this diagram. If we denote distance from the lower Stark electrode by y, and distance measured along this plate by x, then the error is

$$\overline{\frac{\mathscr{E}^2}{(V/d)^2} - 1} = \int\!\!\int \left(\frac{\mathscr{E}^2}{(V/d)^2} - 1\right) dx\, dy$$

where the integral is to be taken over the cross section of the beam. Performing this integration, we find that the error in assuming that the field is constant and equal to $\left(\dfrac{V}{d}\right)^2$ over the cross section of the beam is -1 per cent. A pessimistic estimate for the limits of error for this calculation is ± 0.5 per cent. Therefore we see that this approximate calculation gives an estimate for the homogeneity of the electric field that is in agreement with the electrolytic tank measurements and with the observed fact that the resonance curve linewidth does not increase when the Stark shift is made large.

b. External Magnetic Field

A coil for producing a magnetic field in the transition region was wound around the outside of the main vacuum can. This coil produced a field of approximately one gauss per ampere parallel to the direction of motion of the beam.

3.3 FREQUENCY GENERATION

The source of the stable 9192.6 mc signal for producing the $(4,0) \leftrightarrow (3,0)$ transition was a crystal-stabilized K-band klystron similar to the S-band crystal-stabilized system developed by Searle and McRae (29, 17). This frequency source is described in Appendix IV. This frequency was changed by varying the locking frequency with an automatic-sweep drive.

3.4 FREQUENCY MEASUREMENT

The frequency difference (f_d) between the klystron-output frequency $(f_k \doteq 9192.6$ mc) and the standard frequency $(f_s = 9192.8$ mc) was compared with the 60 cps frequency in the Cambridge electric lines in order to monitor the frequency of the klystron. This comparison was carried out in a circuit that generates a marker pulse (which can be applied to one pen of the Sanborn recorder) every time the frequency changes by 60 cps. This circuit, which we shall call the "frequency indexer" was suggested by Professor J. G. King. It is described in Appendix III.

3.5 RADIOFREQUENCY POWER MEASUREMENT

The relative microwave power that was fed into the transition cavities was monitored with a 20 db directional coupler and a TSX-4SE spectrum analyzer (16). The cavities were matched to the external waveguide feed with a two-slug adjustable X-band tuner located immediately outside the vacuum envelope of the atomic-beam tube. A directional coupler was used to monitor the power reflected from the cavities. The tuner was adjusted to give minimum reflected power. The reflected power was approximately 25 db down from the ingoing power during the Stark effect measurements. The power was controlled with a pair of attenuators between the klystron and the power measurement point. The attenuator on the TSX-4SE spectrum analyzer was used for the measurements of the observed shift as a function of rf power.

3.6 HIGH-VOLTAGE GENERATION AND MEASUREMENT

The Stark voltage was obtained from a supply constructed in this Laboratory. A variac supplies a variable voltage to the primary of a 10 kv transformer. The output of this transformer is rectified with two half-wave Type 8020 rectifiers. This results in two available voltages: zero to +14 kv, and zero to -14 kv. Each of these outputs is filtered by a 0.01 μf condenser with a 400 megohm bleeder chain.

A switch was provided so that each of the Stark electrodes could be charged from one side of this supply through a 9-megohm resistor chain, and so that the Stark electrodes could be grounded.

The voltage applied to the Stark plates was measured with a Rawson Type 518 electrostatic voltmeter (Rawson Electrical Instrument Company, Cambridge, Massachusetts). A switch was provided so that the meter could be connected directly to the positive Stark electrode, and to the negative Stark electrode, or to ground through an 8-megohm resistor chain. This voltmeter was calibrated during the experiment (see Section IV).

IV. EXPERIMENTAL PROCEDURE

4.1 ELECTRIC-FIELD SHIFT AS A FUNCTION OF VOLTAGE

The shift of the observed $(F=4, m_F=0) \leftrightarrow (F=3, m_F=0)$ transition frequency from an electric field applied in the drift space of the transition region was measured for applied voltages from zero to 27 kv. A typical record of the data is shown in Fig. 9. The curves on the right are resonance curves obtained with the Stark voltage off, the curves on the left were obtained with the Stark voltage on. The markers at the lower margin of the recorder chart denote frequency differences of 60 cps. The observed value for the shift can be obtained from these data by counting the number of 60-cps markers between the two resonance peaks.

These data were obtained in the following way (Fig. 7). The frequency of the phase-locked klystron was varied approximately linearly with the automatic-frequency sweep, and the frequency indexer was used to put 60-cps markers on the Sanborn plot. The output of the electron multiplier was recorded on the upper pen of the chart. The middle pen was used to indicate whether or not the Stark voltage was applied to the electrodes. (When this line is up the voltage is on.) With the Stark voltage off, the klystron frequency was swept through the resonance curve; then, with the frequency still drifting in the same direction, the Stark voltage was turned on and a shifted resonance curve was traced out. The voltage applied to the electrodes was measured with the Rawson voltmeter and recorded (with the ingoing rf power) on a separate data sheet. Each pair of curves was given a code number as it was recorded.

At the beginning of each run the power-monitoring system was calibrated with the observed flop by varying the rf power with Stark voltage off, until maximum Ramsey flop amplitude was obtained. The corresponding attenuator reading was then chosen for
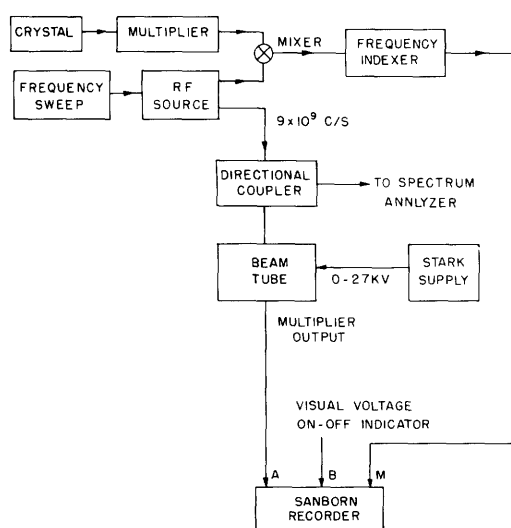

Fig. 7. Experimental procedure for electric-field-shift measurement.

the zero db level. This setting could be made within approximately ±1 db.

After taking one pair of curves, the frequency sweep was reversed and another pair of curves was traced. This tends to eliminate errors arising from long-term crystal drift. The voltage was readjusted and recorded before each pair of curves. Several pairs of curves were taken at each voltage.

In order to guard against possible errors from apparatus variations from run to run, several pairs of curves at 19.9 kv and optimum rf power were observed during each run.

4.2 STARK SHIFT AS A FUNCTION OF RADIOFREQUENCY POWER

To examine the dependence of the observed Stark shift on rf power, pairs of curves were taken for different values of rf power but with the Stark voltage set at a constant value. Several pairs of curves were taken at each power setting. Again, the optimum rf power was determined at the beginning of each run by choosing the zero db point as the point that gave maximum Ramsey amplitude. The spectrum-analyzer-directional-coupler combination was then used to determine the ingoing power relative to this value.

4.3 VOLTMETER CALIBRATION

The data were taken in two groups of three runs each. The voltmeter was calibrated between these two groups of runs. The voltmeter was calibrated at 2-kv intervals against a 0.01 per cent resistor chain, potentiometer, and standard cell. The check points were 0, 2.00, ..., 20.00 kv. The meter-reading correction factors for intermediate voltages were obtained by linear interpolation between the calibration points, but the assumed limits of error for these interpolated correction factors were chosen as one-half of the difference between the two adjacent calibration points, in order to make allowance for the probable inaccuracy of linear interpolation. The voltage errors indicated in the summarized data are the limits of error for the calibration. (The standard deviations of the meter readings for each set of observations made at the same voltage were always less than the calibration errors.) The calibration errors at the calibration points were just the statistical errors associated with reading the meter scale.

4.4 STARK SHIFT AS A FUNCTION OF MAGNETIC FIELD

In order to check a possible dependence of the Stark shift on magnetic field, the shift was observed at different values of external magnetic field with the rf power and the voltage held constant.

The external magnetic field was calibrated by observing the magnetic shift of the $(F=4, m_F=0) \leftrightarrow (F=3, m_F=0)$ transition frequency as a function of the current in the external-magnetic-field coil. Since the frequency for this transition is given by $\Delta\nu(B) = \Delta\nu + 427B^2$ cps, where B is in gauss, this calibration gives the change in the total mean-square magnetic field in the transition region.

18

4.5 PHASE-STABILIZED KLYSTRON STABILITY CHECKS

From time to time, the stability of the klystron stabilization scheme was tested by turning off the frequency sweep on the side of a resonance curve. After several minutes had elapsed the sweep was turned on again and the rest of the resonance curve was traced. The amplitude scale of the recorder plot was calibrated by observing a complete resonance curve with 60-cps markers before and after each stability check.

A typical klystron stability-check data sheet is shown in Fig. 8. The variations in the klystron-output frequency were less than ±20 cps over a period of approximately 7 minutes.
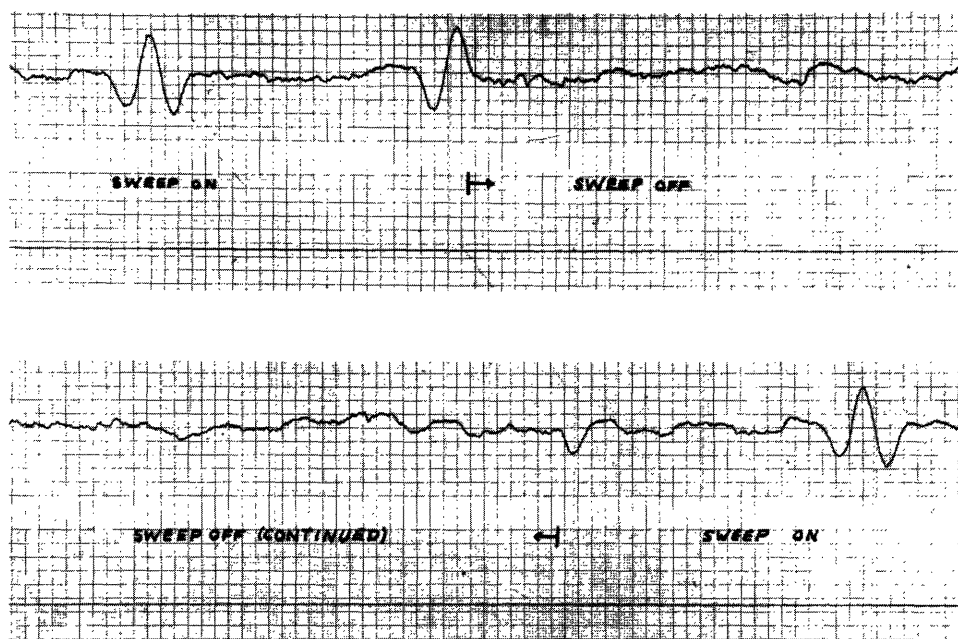
Fig. 8. Frequency-source stability check.

4.6 STARK SHIFT ON FIELD-DEPENDENT TRANSITIONS

An unsuccessful attempt to observe Ramsey flop on a field-dependent high-frequency transition ($\Delta F=1$, $\Delta m_F=1$) was made. Single-cavity flop was observed but the magnetic fields in the transition region could not be adjusted to give Ramsey flop. Essen and Parry (9) have observed this transition with a similar apparatus, and Zacharias, Yates, and Haun have observed field-dependent transitions on the feasibility study test model of the atomic-beam frequency standard. However, we felt that further modifications to the present apparatus would be necessary if these transitions were to be observed. Consequently, attempts to observe these transitions were abandoned.

19

V. RESULTS AND INTERPRETATION OF DATA

5.1 OBSERVED SHIFT AS A FUNCTION OF APPLIED VOLTAGE

The observed frequency difference $\overline{\Delta_o(\mathcal{E})}$ between the peak of the $(4,0)\leftrightarrow(3,0)$ resonance curve with the Stark voltage off and the peak with the voltage on, is tabulated as a function of the square of the applied voltage in Table I. The number of observations made at each voltage setting, the standard deviation of the mean, and the maximum observed deviation from the mean for each set of observations are tabulated. The limits of error given for the voltage measurements are the assumed magnitudes of the calibration errors for the voltmeter.

We note that the greatest maximum deviation from the mean for any observation is 52 cps — the maximum standard deviation of the mean for any set of data is 16 cps. We therefore conclude that the frequency-shift measurements at any voltage setting are self-consistent within better than one per cent.

Table I. Shift of $(4,0)\leftrightarrow(3,0)$ Transition Frequency as a Function of Applied Voltage.

Square of Applied Voltage		Run Number	Observed Shift (Mean)	Standard Deviation of Mean	Maximum Deviation from Mean	Observed Shift Corrected for Asymmetry	Number of Observations	Ratio of Corrected Observed Shift to (Voltage)^2	Error (Per cent)
$(kv)^2$			(cps)	(cps)	(cps)	(cps)		(cps-kv^2)	
V^2	Calibration Error		$\overline{\Delta_o(\mathcal{E})}$			$\overline{\Delta_c(\mathcal{E})}$		$\overline{\Delta_c(\mathcal{E})}/V^2$	
40.4	.5	3	181	2	11	185	15	4.58	1.6
72.4	3.6	3	371	4	30	379	16	5.23	5.1
107.7	2.6	1	542	5	25	555	8	5.15	2.8
108.2	2.5	7	502	4	22	514	8	4.75	2.5
166.1	2.6	3	761	10	24	781	4	4.70	2.1
176.6	4.3	1	783	4	21	804	9	4.55	2.5
211.9	4.7	3	947	6	29	972	8	4.59	2.5
257.9	1.3	1	1216	5	24	1248	8	4.84	.7
267.6	1.3	3	1264	15	15	1297	2	4.85	1.3
320.8	3.6	2	1516	16	16	1557	2	4.85	1.5
333.4	3.7	3	1597	7	31	1640	7	4.92	1.2
397.6	1.6	All	1839	4	49	1889	45	4.75	.5
489.7	4.4	2	2260	8	20	2319	4	4.74	1.0
575.0	1.9	2	2657	4	20	2725	9	4.74	.5
595.4	2.0	6	2776	7	52	2848	10	4.78	.5
637.1	6.1	6	2981	5	15	3056	4	4.80	1.0
692.7	7.3	6	3240	12	45	3323	5	4.80	1.1
748.6	7.7	3	3483	15	40	3569	6	4.77	1.1

A number of typical data records are shown in Figs. 9 and 10 and in Appendix V.

By noting the direction of the frequency sweep for each pair of curves, it was determined that the electric field decreases the observed frequency for the $(4,0)\leftrightarrow(3,0)$ transition from the zero-field value.
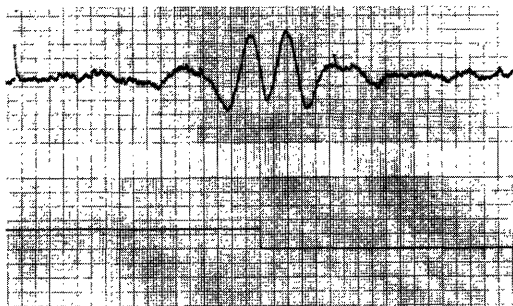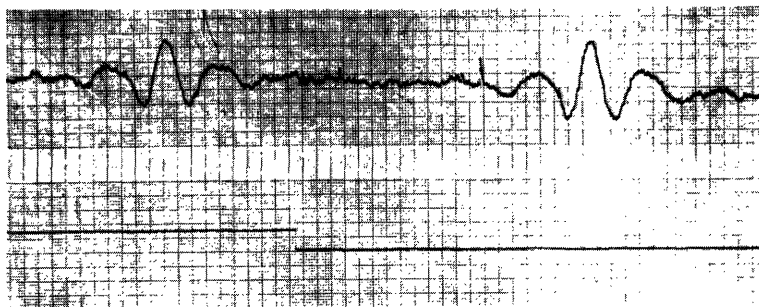
Fig. 9. Typical data recordings. Optimum rf
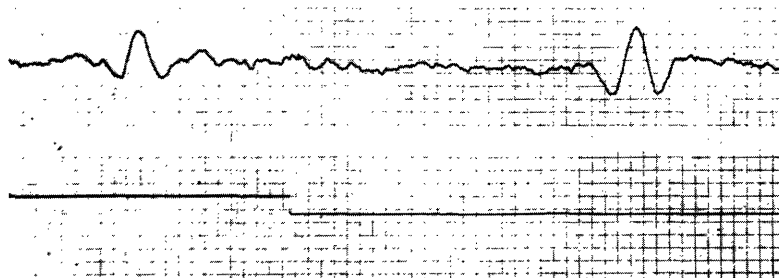power: 22.1 ± .10 kv; 6.35 ± .04 kv.

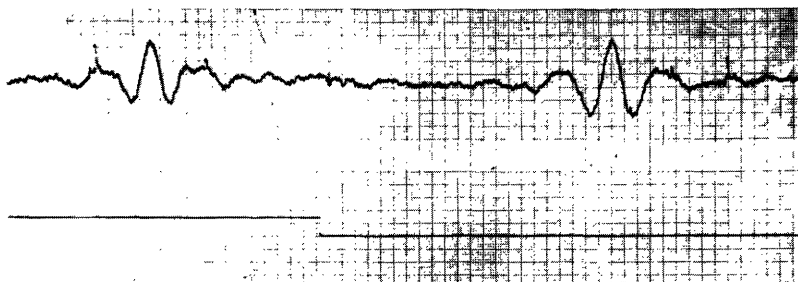Fig. 10. Typical data recordings. Optimum rf power:
Run No. 2, 24.01 ± .04 kv; Run No. 5, 24.49
± .04 kv.

5.2 CHECK POINT

During each run a number of pairs of resonances were observed at optimum rf power and 19.94 kv applied voltage. These observations are tabulated in Table II. The voltmeter was calibrated between runs 3 and 4.

We conclude from these data that measurements from any run agree with the mean of the measurements for all runs within ±1 per cent and that the properties of the voltmeter were not changed more than ±1 per cent during the calibration procedure.

Table II. Check Point.

Run Number	Observed Shift (cps)	Standard Deviation of Mean (cps)	Maximum Deviation from Mean (cps)	Number of Observations
1	1819	4	23	12
2	1854	4	4	4
3	1853	13	26	5
Voltmeter calibrated between runs				
4	1852	8	38	8
5	1834	8	41	8
6	1847	5	22	8

Note: All observations were taken at optimum rf power, with the square of the applied voltage 398 ± 2 kv^2. The runs are in chronological order.
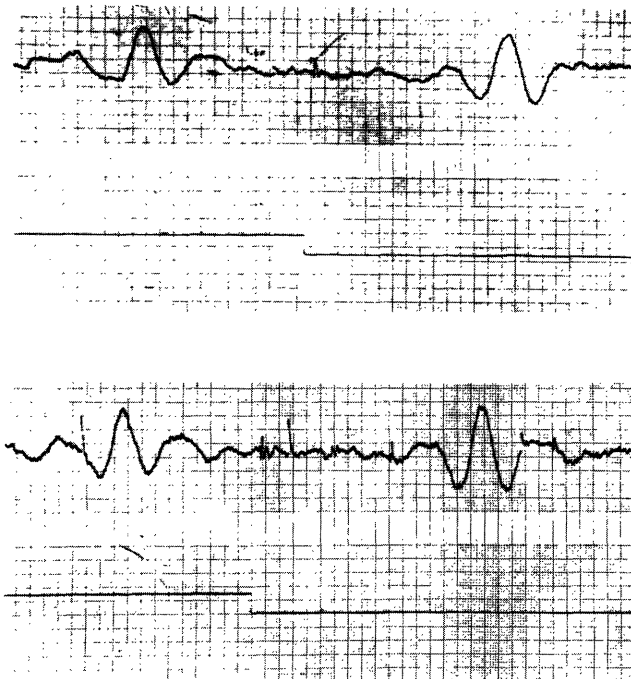
Fig. 11. Typical check-point data recordings. Optimum rf power: Run No. 4, 19.99 ± .04 kv; Run No. 3, 19.80 ± .04 kv.

In Fig. 11 a pair of curves from the first group of runs and a pair of curves from the second group of runs are shown. The signal-to-noise ratios and line shapes for the two groups of runs are approximately the same.

5.3 EXPERIMENTAL TESTS OF THE ASYMMETRY CORRECTIONS

a. Observed Shift as a Function of Power

In order to check the theory for the error in the assumption that the peak of the Ramsey resonance curve corresponds to $\omega = \overline{\omega}_O$, the rf power was varied with the Stark voltage held constant. This was done at voltages corresponding to four values of the observed Stark shift: 0.94×10^3, 1.84×10^3, 2.77×10^3, and 3.45×10^3 cps. The results of these experiments are tabulated in Table III and are summarized graphically

Table III. Observed Shift as a Function of RF Power.

Relative RF Power (db)	Observed Shift (cps)	Standard Deviation of Mean (cps)	Maximum Deviation from Mean (cps)	Number of Observations	Run Number
212 ± 5 kv^2					
-8	930	6	33	10	6
-5	943	6	26	7	6
-2	934	4	24	10	6
0	921	5	20	5	6
0	947	6	29	8	3
1	940	4	24	11	6
2	934	6	36	8	6
398 ± 2 kv^2					
-9	1871	7	38	11	2
-6	1860	6	48	12	1
-3	1844	6	38	12	1
0	1839	4	49	45	All
3	1793	7	52	12	1
3	1780	8	47	8	1
5	1806	6	25	9	2
595 ± 2 kv^2					
-8	2788	4	17	8	4
-5	2764	7	21	5	4
-2	2789	8	33	8	4
0	2776	7	31	10	4
2	2770	6	19	8	4
4	2720	8	46	4	4
742 ± 8 kv^2					
-5	3463	8	41	9	4
-2	3431	5	21	9	4
0	3452*	15	40	6	3
1.5	3444	6	29	12	4
4	3432	5	25	9	4

*This observation was actually 3483 cps at 749 kv^2 but it was reduced to the value given in this table by multiplying by the ratio of the squares of the voltages.
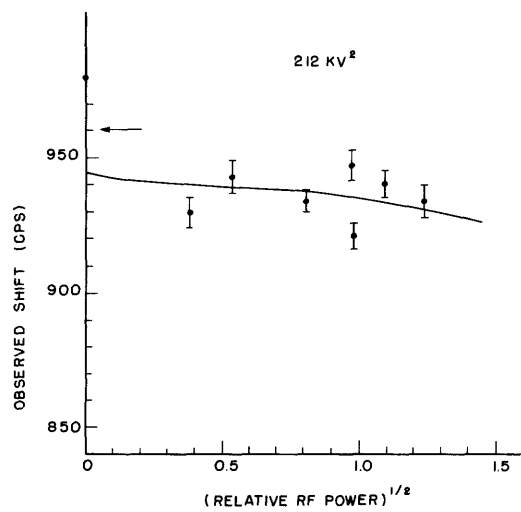
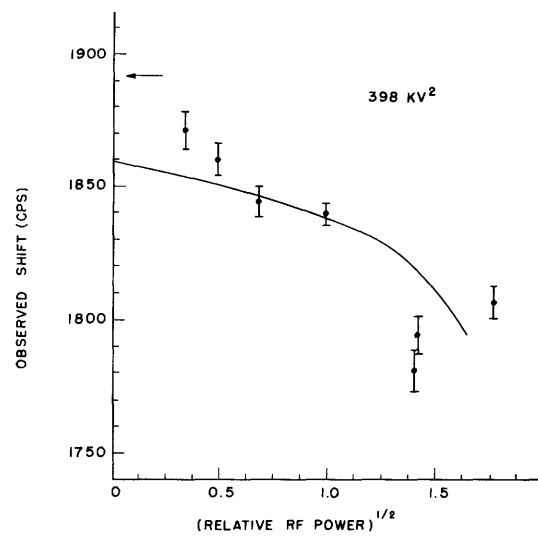Fig. 12. Observed shift as a function of rf power (212 kv^2).

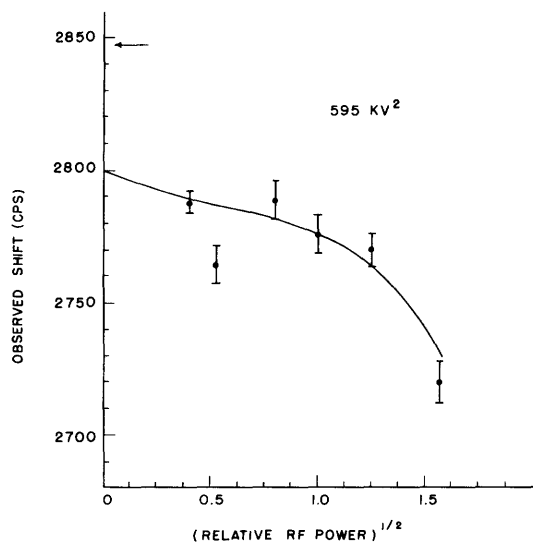Fig. 13. Observed shift as a function of rf power (398 kv^2).

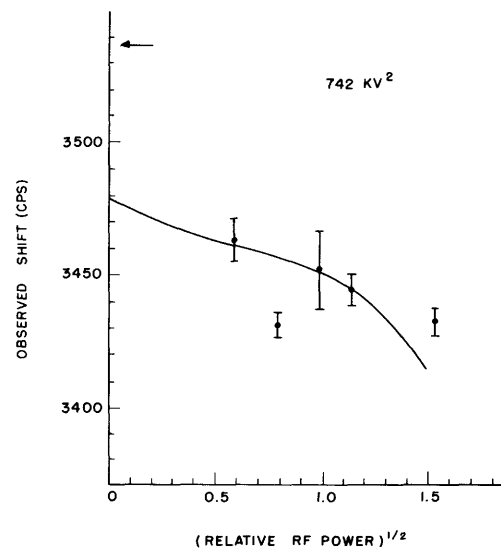Fig. 14. Observed shift as a function of rf power (595 kv^2).

Fig. 15. Observed shift as a function of rf power (742 kv^2).

24

in Figs. 12, 13, 14, and 15. The solid lines represent the theoretically derived variation of the observed shift with power for the velocity distribution which was obtained from the apparatus dimensions (Appendix II and section 2.4). The only arbitrary parameter used for obtaining the shape of the theoretical curves is $a = 1.8 \times 10^4$ cm/sec. (See Appendix II.) This value of a gives the values $b_o = 2.06 \times 10^3$ cps, and $\gamma = \frac{\delta}{74}$, where δ is in cps.

Since the theory only predicts shifts from the zero-power level, the frequency zero of the theoretical curve was arbitrarily chosen to give agreement between theory and experiment at the optimum power point ($b/b_o = 1$). This is the choice that is made in section 5.5, in which the observed shift is corrected for the asymmetry due to $\omega_o \neq \overline{\omega}_o$. The value of the Stark shift corrected for the asymmetry is indicated by an arrow on each figure.

From Figs. 12, 13, 14, and 15 we conclude that, although the fit of the experimental data to the theoretical curves is not sufficiently good to guarantee the validity of the asymmetry calculations, there does seem to be agreement within ±1 per cent of the total observed Stark shift.

The theoretically derived velocity distribution was used for the curves in these figures because it gives slightly better agreement with the data than does the $v^3 e^{-\left(\frac{v}{a}\right)^2}$ distribution. However, the maximum difference between the two distributions is only about five cps so that the choice of velocity is not significant as far as this experiment is concerned.

b. Line Shapes

As a further test of the agreement of the asymmetry theory with experiment we can compare experimental and theoretical line shapes.

In Fig. 16 the experimental line shape for optimum rf power and no electric field is plotted for comparison with the theoretical line shapes predicted for the two velocity distributions, with the use of the values of a given in Appendix II. (These values of a were chosen to give the observed linewidths for the central Ramsey peak. The value of a used for the distribution derived from the apparatus dimensions is the same as that used for the curves of observed shift as a function of power and for the asymmetrical line-shape comparisons that will be discussed later.) The $v^3 e^{-\left(\frac{v}{a}\right)^2}$ distribution seems to give a slightly better fit on the subsidiary peaks than does the distribution derived from the apparatus dimensions, but the noise level (indicated by the bars in Fig. 16) is not sufficiently good to make possible a definite choice.

In Fig. 17 the experimental line shape for an observed Stark shift of 1.9×10^3 cps and twice optimum rf power ($b/b_o = 1.4$) is compared with the line shape for similar conditions predicted by the Ramsey formula by using the theoretically derived velocity distribution with $a = 1.8 \times 10^4$ cm/sec. Two typical data records for these experimental conditions are shown in Fig. 18. In Fig. 17 the zero of the frequency scale for
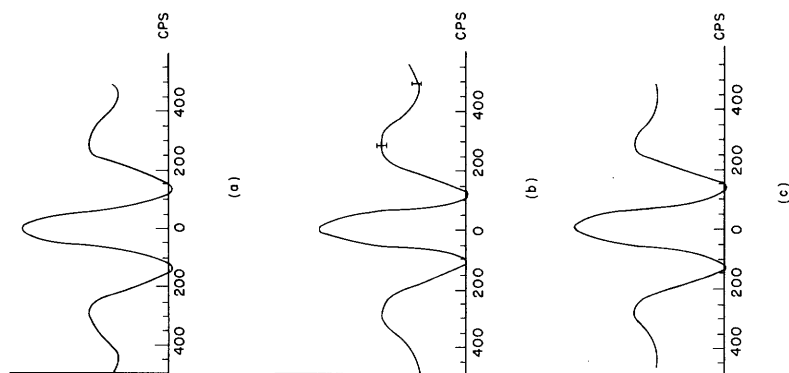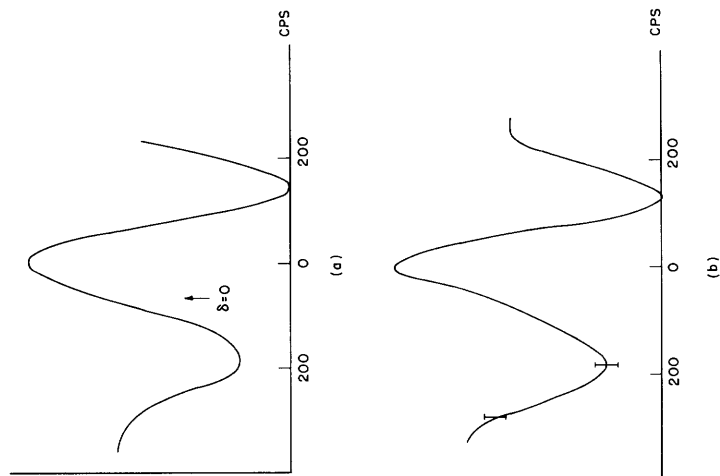
Fig. 17. Theoretical and experimental line shapes. Observed shift $\doteq 1.9 \times 10^3$ cps; (a) derived distribution $b/b_o = 1.4$; (b) experimental +3 db power.
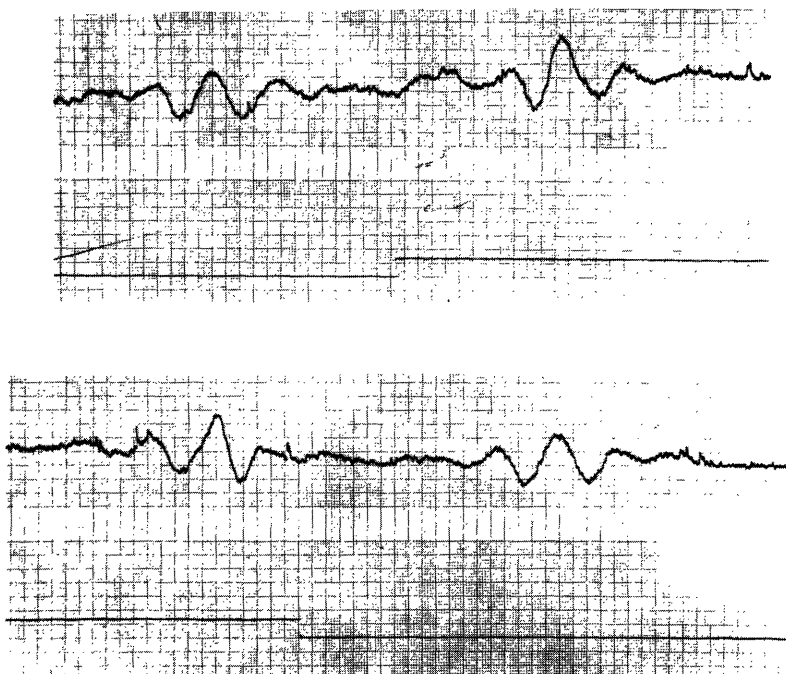

Fig. 16. Theoretical and experimental line shapes (zero electric field): (a) $v^3 \exp[-(v/\alpha)^2]$; derived distribution $b/b_o = 1.0$; (b) experimental optimum power; (c) derived distribution $b/b_o = 1.0$.

Fig. 18. Typical data recordings (rf power + 3 db): Run No. 1,
19.87 ± .04 kv (frequency decreasing toward right);
19.90 ± .04 kv (frequency increasing toward right).

the theoretical curve has been chosen so as to make the peaks of the two curves coincide; the position of the peak corrected for the asymmetry is indicated by an arrow. The agreement between the theoretical and experimental line shapes is remarkably good as far as the two "valleys" are concerned; the agreement at the subsidiary peaks is not as good. This is to be expected, since the parts of the curve close to the central peak are less dependent on the form of the velocity distribution than the parts of the curve which are further out. From the agreement of the curves, we conclude that the asymmetry theory is in good agreement with the experimentally observed line shape and that the Stark field is homogeneous over the width of the beam.

5.4 OBSERVED SHIFT AS A FUNCTION OF MAGNETIC FIELD

The measurements of the observed Stark shift for two values of applied voltage at several different values of external magnetic field are summarized in Table IV. From these data we conclude that the Stark shift on the $(4, 0) \leftrightarrow (3, 0)$ hyperfine-structure separation is independent of the magnetic field within ±1 per cent at 398 kv^2, and within ±2 per cent at 108 kv^2, for magnetic fields less than four gauss.

We therefore conclude that, since the total magnetic field in the transition region (with no current in the external field coil) is less than one gauss, no error in the measurement of the Stark shift in this experiment results from the fact that the value

27

of the magnetic field in the transition region is not known exactly.

Table IV. Observed Shift as a Function of Magnetic Field.

Change in RMS Magnetic Field (gauss)	Observed Shift (cps)	Standard Deviation of Mean (cps)	Maximum Deviation from Mean (cps)	Number of Observations	Run Number
$398 \pm 2 \text{ kv}^2$					
0.0	1853	14	26	5	3
0.0	1847	5	22	8	6
0.4	1861	7	16	4	6
1.0	1845	10	22	4	3
1.5	1843	9	37	8	6
2.4	1860	9	38	8	3
3.4	1848	6	32	8	6
4.4	1852	9	26	6	6
4.4	1843	9	40	8	3
$108 \pm 3 \text{ kv}^2$					
0.0	502	4	22	8	7
1.0	497	5	23	8	7
2.4	516	2	9	8	7
4.4	509	4	16	8	7

Note: All observations were made at –1 db rf power.

5.5 OBSERVED SHIFT CORRECTED FOR ASYMMETRY

Assuming that the theoretical correction for asymmetry due to $\omega_o \neq \overline{\omega}_o$, with the velocity distribution derived from the apparatus dimensions (Appendix II), is correct, the observed values of the shift caused by the electric field were corrected, as shown in column 7 of Table I. The theoretical parameter used in calculating the correction from Fig. 3 is $a = 1.8 \times 10^4$ cm/sec. $\left(\text{This value of } a \text{ gives } b_o = 2.06 \times 10^3 \text{ cps, and } \gamma = \frac{\delta}{74}. \right)$

These corrected values are plotted as a function of the square of the applied voltage in Fig. 19. The solid line is the weighted mean ratio of the corrected shift $\overline{\Delta_c(\mathscr{E})}$ to the square of the applied voltage (V^2), where the ratio for each value of V^2 in Table I has been weighted with the reciprocal square of its percentage of error (W1). (This error includes statistical errors and the calibration error of the meter.) The equation of this line is

$$\overline{\overline{\Delta_c(\mathscr{E})}} = 4.77 \text{ V}^2 \text{ cps}$$

where V is in kilovolts.

We conclude from Fig. 19 that the data fits the assumption of a quadratic Stark shift within the experimental error (approximately 1 per cent) and that this shift
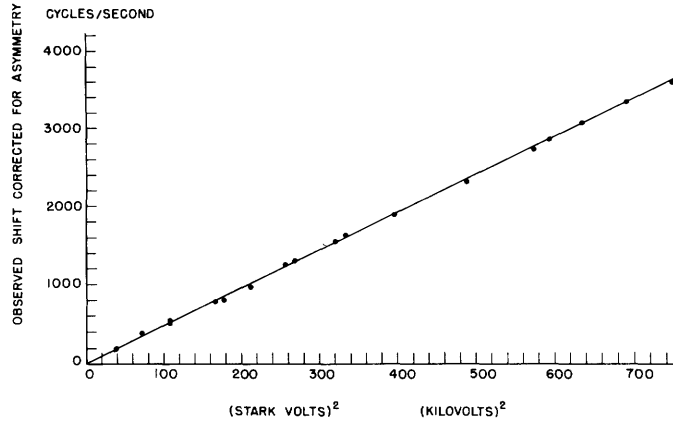
Fig. 19. Corrected observed shift of $(4, 0) \leftrightarrow (3, 0)$ transition as a function of the square of the applied voltage.

is given by

$$\overline{\Delta_c(\mathscr{E})} = 4.77 \ V^2 \ (1 \pm .01) \ \text{cps}$$

where V is in kilovolts.

5.6 SHIFT OF THE HYPERFINE-STRUCTURE SEPARATION AS A FUNCTION OF ELECTRIC FIELD

a. Correction from Observed Shift to Shift of Transition Frequency

Since the peak of the Ramsey resonance curve (corrected for the asymmetry due to $\omega_0 \neq \overline{\omega}_0$) occurs at the frequency corresponding to the mean transition frequency averaged over the drift region between the two transition cavities, the shift $\Delta_v(\mathscr{E})$ of the hyperfine-structure separation frequency is related to the observed shift by

$$\Delta_v(\mathscr{E}) = \overline{\Delta_c(\mathscr{E})} \ \frac{L}{L_{\text{Stark}}}$$

where L_{Stark} is the effective length of the electric field region, as it was previously defined, and L is the distance between the two rf cavities.

In this experiment $L = 78.4 \pm 0.2$ cm and $L_{\text{Stark}} = 66.0 \pm 0.2$ cm, so that

$$\Delta_v(\mathscr{E}) = \frac{78.4}{66.0} \ \overline{\Delta_c(\mathscr{E})}$$

$$= 5.68 \ (1 \pm 0.01) \ V^2 \ \text{cps}$$

where V is in kilovolts.

b. Calculation of Electric Field from Applied Voltage

Since the separation of the Stark electrodes is $0.635 \pm .006$ cm, the square of the electric field $\mathscr{E}$ can be obtained from the applied voltage V by

29

$$\mathcal{E}^2 = \frac{V^2}{0.403} \ (1 \pm .02) \ kv^2/cm^2$$

where V is in kilovolts. In this calculation we have neglected the inhomogeneity of the electric field across the beam. Since the field is homogeneous only within ± 1 per cent, we obtain

$$\mathcal{E}^2 = \frac{V^2}{0.403} \ (1 \pm .022) \ kv^2/cm^2$$

c. Value for the Shift with All Corrections

Combining the calculations, we obtain

$$\Delta(\mathcal{E}) = 2.29 \times 10^{-6} \ (1 \pm .025) \ \mathcal{E}^2 \ cps$$

where $\mathcal{E}$ is in volts/centimeter.

VI. SUMMARY AND DISCUSSION

The shift of the $(4, 0) \leftrightarrow (3, 0)$ energy separation in cesium[133] caused by an electric field $\mathscr{E}$ is given by

$$\Delta(\mathscr{E}) = -2.29 \times 10^{-6} \ (1 \pm .03) \ \mathscr{E}^2 \text{ cps}$$

where $\mathscr{E}$ is in volts/centimeter. This measured value is independent of magnetic field within 1 per cent for fields of less than four gauss.

The principal sources of error in this determination and their estimated magnitudes are:

a. Statistical Errors:

1. Frequency source instability (less than ± 10 cps at 9192 mc during the time required for a measurement).

2. Instability of the Cambridge 60-cps lines (less than one part in 10^4 of 60 cps).

3. Beam noise (equivalent to less than ± 10 cps).

4. Voltmeter calibration and scale-reading errors (see Table I).

The estimated total error from all of these sources is ± 1 per cent.

b. Systematic Errors:

1. Separation of Stark electrodes (distance known within ± 1 per cent), ± 2 per cent.

2. Stark-field homogeneity, ± 1 per cent.

3. Ramsey asymmetry correction, ± 1 per cent.

i. Velocity-independent part. (This part of the correction is $1.6 \pm .1$ of the observed shift.)

ii. Velocity-distribution-dependent part. (This part of the correction is known within approximately ± 10 cps.)

The estimated total error, including systematic and statistical errors, is therefore ± 2.5 per cent.

The polarizability measurements of Scheffers and Stark, combined with the theory of section 2.2, give

$$\Delta(\mathscr{E}) = -0.82 \times 10^{-6} \ (1 \pm .05) \ \mathscr{E}^2 \text{ cps}$$

Thus far no comparison can be made without a more precise theory for taking into account the difference between the F=4 and the F=3 wave functions.

THEORY OF THE STARK EFFECT ON HYPERFINE STRUCTURE

Schwartz (26) has recently suggested the following analysis for the effect of an electric field on the hyperfine-structure energy separation:

Consider the Hamiltonian $H = H_o + H_1$, where H_o is that part of the total energy of the atom which includes coulomb and fine-structure interactions only, and H_1 is the perturbation from hyperfine structure and the interaction of the atom with an external electric field. (As discussed in section 2.2, the magnetic perturbation for the $m_F = 0$ levels in the cesium[133] ground state is small in comparison with H_1, so that magnetic effects can be neglected here.)

Let us write H_1 as

$$H_1 = H_{hfs} + ez\mathscr{E}$$

where H_{hfs} is the hyperfine-structure perturbation, and $ez\mathscr{E}$ is the perturbation caused by the electric field.

We now apply conventional perturbation theory to H_1. Let us consider the special case of cesium[133] which has a 6s ground state and a nuclear spin 7/2. Let us choose the F representation for the wave functions, where F is the magnitude of the vector sum of the total electronic angular momentum J and the nuclear angular momentum I.

1. In first order we obtain

$$E_F^{(1)} = \langle n=6, L=0, F | H_{hfs} | n=6, L=0, F \rangle + \langle 6, 0, F | ez\mathscr{E} | 6, 0, F \rangle$$

But, since z has odd parity and the 6s state has definite parity, the diagonal matrix elements of $ez\mathscr{E}$ vanish. We therefore obtain

$$E_F^{(1)} = \langle n=6, L=0, F | H_{hfs} | n=6, L=0, F \rangle$$

which gives the usual hyperfine-structure levels (3).

2. In second order we obtain

$$E_F^{(2)} = + \sum_{n'L'F'}{}' \frac{\langle 60F | H_1 | n'L'F' \rangle \langle n'L'F' | H_1 | 60F \rangle}{W^o(n=6, L=0) - W^o(n=n', L=L')}$$

$$= \sum_{n'L'F'}{}' \frac{| \langle 60F | H_{hfs} | n'L'F' \rangle |^2}{W^o(60) - W^o(n'L')}$$

$$+ \sum_{n'L'F'}{}' \frac{2 \langle 60F | H_{hfs} | n'L'F' \rangle \langle n'L'F' | ez\mathscr{E} | 60F \rangle}{W^o(60) - W^o(n'L')} +$$

$$+ \sum_{n'L'F'}^{'} \frac{|<60F|ez\mathscr{E}|n'L'F'>|^2}{W^o(60) - W^o(n'L')}$$

The first term gives a field-independent correction to the hyperfine-structure levels. The third term represents the usual second-order Stark effect — as measured by Scheffers and Stark — in which both hyperfine-structure levels are shifted by the same amount. The second term is zero because the hyperfine-structure perturbation is of even parity and the electric field perturbation is of odd parity.

3. In third order we obtain (4)

$$
\begin{aligned}
E_F^{(3)} = \sum_{\substack{n'L'F' \\ n''L''F''}} & \left[\frac{<60F|H_{hfs}|n'L'F'> <n'L'F'|H_{hfs}|n''L''F''> <n''L''F''|H_{hfs}|60F>}{(W^o(60) - W^o(n'L')) (W^o(60) - W^o(n''L''))} \right. \\[2ex]
& + \frac{<60F|H_{hfs}|n'L'F'> <n'L'F'|ez\mathscr{E}|n''L''F''> <n''L''F''|H_{hfs}|60F>}{(W^o(60) - W^o(n'L')) (W^o(60) - W^o(n''L''))} \\[2ex]
& + \frac{<60F|H_{hfs}|n'L'F'> <n'L'F'|H_{hfs}|n''L''F''> <n''L''F''|ez\mathscr{E}|60F>}{(W^o(60) - W^o(n'L')) (W^o(60) - W^o(n''L''))} \\[2ex]
& + \frac{<60F|ez\mathscr{E}|n'L'F'> <n'L'F'|H_{hfs}|n''L''F''> <n''L''F''|ez\mathscr{E}|60F>}{(W^o(60) - W^o(n'L')) (W^o(60) - W^o(n''L''))} \\[2ex]
& + \frac{<60F|ez\mathscr{E}|n'L'F'> <n'L'F'|H_{hfs}|n''L''F''> <n''L''F''|H_{hfs}|60F>}{(W^o(60) - W^o(n'L')) (W^o(60) - W^o(n''L''))} \\[2ex]
& + \frac{<60F|ez\mathscr{E}|n'L'F'> <n'L'F'|ez\mathscr{E}|n''L''F''> <n''L''F''|H_{hfs}|60F>}{(W^o(60) - W^o(n'L')) (W^o(60) - W^o(n''L''))} \\[2ex]
& + \frac{<60F|H_{hfs}|n'L'F'> <n'L'F'|ez\mathscr{E}|n''L''F''> <n''L''F''|ez\mathscr{E}|60F>}{(W^o(60) - W^o(n'L')) (W^o(60) - W^o(n''L''))} \\[2ex]
& \left. + \frac{<60F|ez\mathscr{E}|n'L'F'> <n'L'F'|ez\mathscr{E}|n''L''F''> <n''L''F''|ez\mathscr{E}|60F>}{(W^o(60) - W^o(n'L')) (W^o(60) - W^o(n''L''))} \right] \\[2ex]
& - <60F|H_{hfs}|60F> \sum_{n'L'F'} \frac{|<60F|ez\mathscr{E}|n'L'F'>|^2}{(W^o(60) - W^o(n'L'))^2}
\end{aligned}
$$

Terms of the form $<|H_{hfs}|> \; <|H_{hfs}|> \; <|ez\mathscr{E}|>$ will be zero because H_{hfs} is an even operator and $ez\mathscr{E}$ is an odd operator. The term involving the three $ez\mathscr{E}$ matrix elements can be neglected because it is smaller than the other terms by quantities of the order

$$\frac{<|ez\mathscr{E}|>}{<|H_{hfs}|>}$$

The first term (which involves the three H_{hfs} matrix elements) is just another field independent correction to the hyperfine-structure energy levels.

The final result is that, in so far as the electric-field dependence is concerned, the F-levels are each shifted by an amount

$$E_F^{(3)} = - \sum_{\substack{n'L'F' \\ n''L''F''}} \frac{1}{(W^o(60) - W^o(n'L'))(W^o(60) - W^o(n''L''))} \; .$$

$$[<60F|H_{hfs}|n'L'F'> \; <n'L'F'|ez\mathscr{E}|n''L''F''> \; <n''L''F''|ez\mathscr{E}|60F>$$

$$+ \; <60F|ez\mathscr{E}|n'L'F'> <n'L'F'|H_{hfs}|n''L''F''> \; <n''L''F''|ez\mathscr{E}|60F>$$

$$+ \; <60F|ez\mathscr{E}|n'L'F'> < \; n'L'F'|ez\mathscr{E}|n''L''F''> \; <n''L''F''|H_{hfs}|60F>]$$

$$- \; <60F|H_{hfs}|60F> \sum_{n'L'F'} \frac{|<60F|ez\mathscr{E}|n'L'F'>|^2}{(W^o(60) - W^o(n'L'))^2}$$

In the order-of-magnitude calculation outlined in section 2.2, only the last term of $E_F^{(3)}$ was considered. The other three terms can be of comparable magnitude.

Since numerical evaluation of the matrix elements involved in the aforementioned expression is rather complicated for cesium, an explicit solution was not completed for this report. C. H. Schwartz has indicated that he may attempt a solution of this problem.

34

APPENDIX II

OFFSET GEOMETRY AND VELOCITY DISTRIBUTION

During the work on the feasibility-study test model (34) it was found that a consider-able reduction in resonance-curve halfwidth could be obtained by displacing the source and detector to opposite sides of the axis of the apparatus. This reduction in linewidth occurs because the offset geometry makes it possible to use the entire gap of the deflecting magnets rather than one-half of the gap, as is the case for conventional axial line-up. The greater effective gap width means that atoms of lower velocity can get through the deflecting magnets without being cut off by the magnet pole faces. Offset geometry has a further advantage in that the detector can be shielded from the source with the magnet pole faces so that atoms that do not undergo transitions between the two deflecting magnets cannot reach the detector, unless they are scattered from some surface or by gas collisions.

In the feasibility-study test model the use of offset geometry was desirable because of the excessive length (10 inches) and small gap width (0.125 inch) of the deflecting magnets. These dimensions so limited the deflections that atoms of less than the mean velocity of the Maxwellian distribution (corresponding to the source temperature) were stopped by the deflecting magnet pole faces. The use of offset geometry resulted in a reduction in linewidth from 360 cps (for axial geometry) to 200 cps, and also gave an improvement in signal-to-noise ratio. However, the use of offset geometry so reduced the velocity spread of the beam that the cancellation of the subsidiary Ramsey peaks was very poor and as many as 15 peaks were observed in the resonance pattern (34).

In the apparatus described in this report the magnets were made short (3.5 inches) and the gaps were made wide (0.250 inch), so that offset geometry could be used to the fullest advantage. The result was a linewdith of 120 cps, with only two small subsidi-ary peaks.

Since the positions of all components of the apparatus inside the vacuum enclosure are fixed while the system is under vacuum, it was necessary to make rather detailed calculations of the line-up parameters. Since the form of the velocity distribution is of importance in the theory for the asymmetry of the Ramsey resonance curve (section 2.4), the line-up calculations (which yield the velocity distribution) will be outlined in some detail.

Let us assume that the positions of the source and deflecting magnets are known. Assume that the source beam-slit assembly (see section 3.2) has width d, and that the angular spread of the beam as it leaves the source tubes is 2θ radians. We can then approximate the shape of the undeflected beam by a trapezoid that has an umbra d cm wide and a penumbra that subtends the angle θ at the source.

To calculate the distribution of the beam in the plane of the detector as a function of velocity, we proceed as follows.

1. For a single velocity v, we calculate the location of one side of the umbra at various points along the length of the apparatus (for example, at the source end of the second deflecting magnet). The umbra at each of these points will, of course, be d cm wide, but its location relative to the axis of the apparatus will be determined by the deflections that the atoms undergo in the deflecting magnets.

2. For a single velocity, we find the limits of the penumbra at each of the points just considered. If the point is L cm from the source, and the position of the side of the umbra is y_O, then the limits of the penumbra are at $y_O - L\theta$ and at $y_O + d + L\theta$.

3. We now consider the effects of the collimating edges in the apparatus (for example, the edges of the pole faces of the deflecting magnets). If an edge L cm from the source intercepts the beam at some value of y, then, for all points closer to the detector, we use the new penumbra angle $\theta' = d/[L + (d/\theta)]$ for the parts of the beam that lie farther from the axis than y at L. (For parts of the beam that are closer to the axis than y at L, we use the penumbra angle θ, since these parts of the beam are not affected by the collimating edge.)

4. We proceed from source to detector in this way until the detector plane is reached. Then we have the distribution of atoms with the velocity v in the detector plane. These calculations are made for atoms that undergo transitions ("flopped" atoms) and for those that do not ("unflopped" atoms).

5. The same calculations are repeated for different values of v.

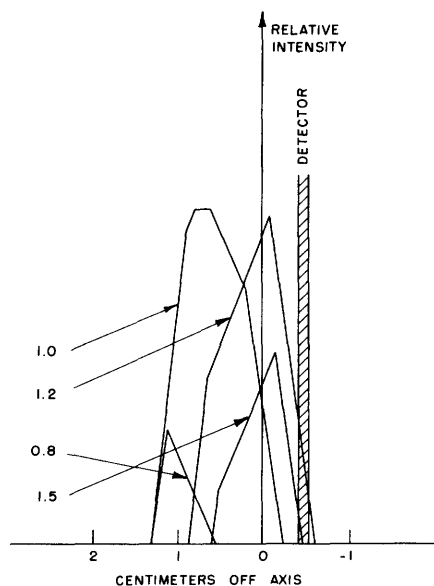Having thus obtained a complete picture of the flopped and unflopped beam in the

Fig. 20. Offset-geometry distribution of unflopped atoms in detector plane.
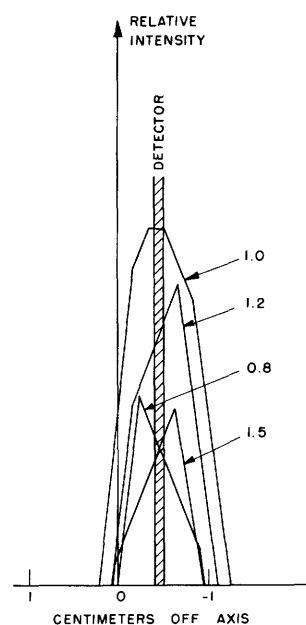

Fig. 21. Offset-geometry distribution of flopped atoms in detector plane.

detector plane as a function of velocity, we choose the position of the source so that it intercepts the most flopped beam, the least unflopped beam, and the widest spread of velocities.

In carrying out these calculations it was found that most of the beam cutoff occurs at the source end of the second deflecting magnet, with the detector end of each of the magnets playing a much smaller role.

For the apparatus described in this report, it was determined (by repeated calculation) that at the optimum source position the edge of the penumbra for infinite-velocity atoms just grazes the far edge of the detector end of the second deflecting magnet. The deflecting magnets were both tilted through half the angle between the line connecting the source slit and the center of the first deflecting-magnet gap. The optimum detector position was found as outlined above, with the assumption that the source parameters were $d = 0.15$ cm and $\theta = 0.01$ radian.

Figures 20 and 21 show the calculated distributions in the detector plane of flopped and unflopped beams of various velocities, for the apparatus dimensions shown in Fig. 4. The numbers on each curve denote the ratio of the velocity for that curve to the velocity v_o of the atoms whose umbra moves parallel to the axis of the apparatus in the transition region. All of the curves were normalized to the same maximum value, which had been chosen as unity.

In order to obtain the weighting factors (for the detected signal) resulting from the deflections and cutoff edges as a function of velocity, we simply take the difference in the ordinates of the flopped and unflopped curves at the detector position.

Since the velocity distribution of the atoms leaving the source is given by $v^3 \exp[-(v/a)^2]$, we must weight the weighting factors obtained in the calculation above with the $v^3 \exp[-(v/a)^2]$ distribution corresponding to the source temperature (Fig. 22).

The theoretical velocity distribution that results from these calculations, as applied to the apparatus shown in Fig. 4, is shown in Fig. 23. Since tables of the function I(m)
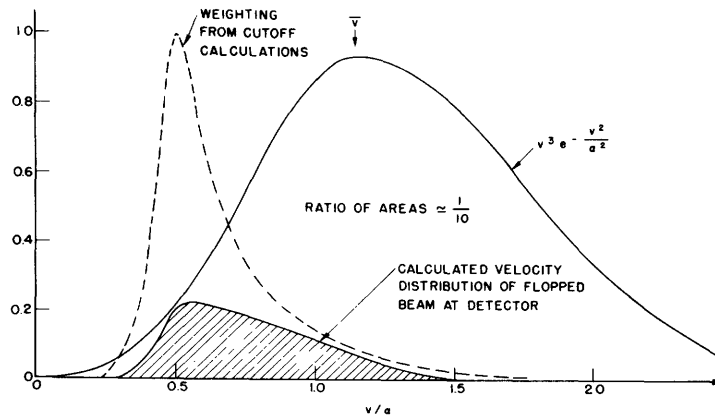

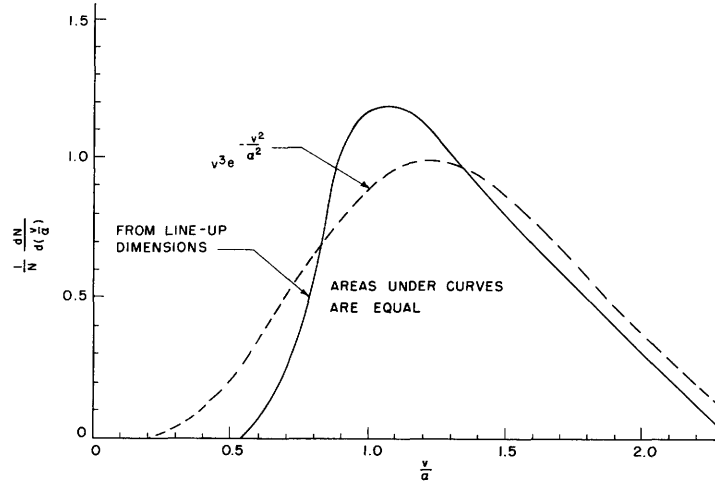Fig. 22. Offset-geometry distribution of flopped beam.

37

Fig. 23. Comparison of derived theoretical and
$v^3 \exp(-v/a)^2$ velocity distributions.

exist (19) for the $v^3 \exp[-(v/a)^2]$ distribution, it was possible to plot a distribution of this form in Fig. 23 for comparison with the theoretically derived distribution. (Note that the parameter a used in plotting these curves is not the most probable velocity for the source temperature. Instead, it is the most probable velocity for the $v^3 \exp[-(v/a)^2]$ distribution that gives approximately the same linewidth as the theoretically derived distribution.) The areas under the two distributions are equal. The fit of the two distributions is seen to be very good for $v \gtrsim a$, but there are fewer low-velocity atoms in the theoretically derived distribution than in the $v^3 \exp[-(v/a)^2]$ distribution. This is not surprising, since the slow atoms are the ones that are most likely to strike the pole faces because of their large deflections.

We can approximate the theoretically derived velocity distribution by the function

$$\frac{dN}{d\left(\frac{v}{a}\right)} = \begin{cases} 0 & \text{for} & 0.6 \geqslant v/a \geqslant 2.3 \\ 3.25\frac{v}{a} - 1.95 & \text{for} & 0.6 \leqslant v/a \leqslant 1.0 \\ 2.30 - \frac{v}{a} & \text{for} & 1.0 \leqslant v/a \leqslant 2.3 \end{cases}$$

Tables of the function I(m) for this velocity distribution were prepared by the Joint Computation Group, M.I.T., and are on file there.

In order to obtain the experimentally observed Ramsey linewidth of 120 cps (for optimum power with no Stark field), the parameter a must be given the following values:

1. For the theoretical distribution, $a = 1.8 \times 10^4$ cm/second.

2. For the $v^3 \exp[-(v/a)^2]$ distribution, $a = 1.7 \times 10^4$ cm/second.

The assumption of the value $a = 1.8 \times 10^4$ cm/sec, combined with the known source position, gives the value 9.1×10^3 gauss for the field at the convex pole face of the

38

deflecting magnet. This is in fair agreement with the measured value of 8.6×10^3 gauss.

The values of a given above were the only "arbitrary" parameters used in the Ramsey asymmetry calculations of Section V. (See Fig. 16 for a comparison of the theoretical line shapes with the experimentally observed line shape.)

APPENDIX III

DESCRIPTION OF APPARATUS

In this appendix the various components of the apparatus used for the Stark-shift experiment are described in detail.

1. BEAM TUBE

The general arrangement of the components that are inside the vacuum is shown in Fig. 4. (See section 3.2 for a description of the Stark electrodes.)

a. Vacuum System

The cesium sources, deflecting magnets, detectors, and the high-frequency transition cavities are all mounted on a pair of aluminum U-channels. The entire assembly is enclosed in a vertical, cylindrical vacuum chamber that was kept at a pressure of 1 to 4×10^{-7} mm Hg during the measurements. This vacuum system was designed by Professor J. R. Zacharias.

The main can is a vertical stainless steel tube, 10 inches in diameter and 6 feet high. The U-channels are lowered into the upper end of the tube and a soft-solder joint is made between the portion of the can which is attached to the channels and the tube proper.

The electric connections to the inside of the can are made through ceramic-seal troughs soldered to a large brass plate that serves as the top end of the vacuum chamber. The channels are bolted to this plate.

The main vacuum tube is connected to the pumps through a stainless steel tube 6 inches in diameter and 10 inches long. The General Electric Company type ion gauge used to monitor the pressure is located on this tube.

The main diffusion pump is a Consolidated Vacuum Corporation MCF-300-01 pump. The booster pump is an MCF-60-01 pump. Both of these pumps were filled with Octoil pump fluid which had been in use for 10 months when the last run was made. A Welch Duo-seal mechanical pump was used as the forepump.

Directly above the large diffusion pump (and at the end of the 6-inch tube) is a liquid nitrogen trap. The capacity of this trap is approximately 1.5 liters. Surrounding this trap is a vacuum jacket that is part of the evacuated system, and surrounding this vacuum jacket is a dry-ice trap that will hold approximately 40 pounds of dry ice. During one vacuum test there was still a measurable amount of liquid nitrogen in the trap 57 hours after both traps had been filled.

b. Source of Cesium Atoms

A cesium atomic-beam source consists of a hollow block of metal inside of which is placed the material that is used to produce the beam. When this block of metal is heated, the cesium atoms effuse out through a source slit that connects the interior of the source
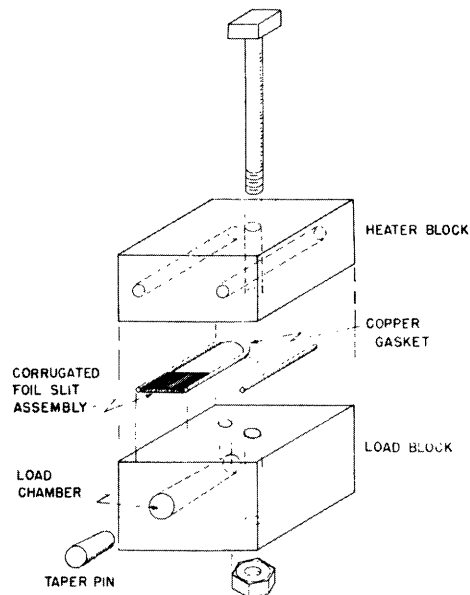
Fig. 24. Corrugated-foil cesium atomic-beam source.

with the surrounding vacuum. These atoms form the beam.

The source design for this experiment is shown in Fig. 24. This source consists of two stainless steel blocks between which is placed a "crinkly foil" source-tube assembly (34). (See also Appendix IV.) The dimensions of the source-tube assembly are 0.040 X 0.5 inch. The tubes are 0.5 inch long. The corrugations are approximately 0.002 inch deep. To prevent leakage around this assembly, a copper wire is used as a gasket. The two blocks are held together with a 0.25-inch stainless bolt which passes through the centers of the two blocks. The material used to generate the beam is placed in a cavity inside one of the two blocks. This cavity is connected to the source-tube assembly through a 0.125-inch hole in the block. The loading hole is plugged with a copper-plated taper pin which can be removed with a bolt and jack when the source is to be reloaded.

The source is heated ohmically by two molybdenum heaters inserted in one of the blocks. The current for these heaters is obtained from a variac-controlled 12-volt ac supply. The temperature of the source was monitored by an iron-constantan thermo-couple which was inserted in a hole in the same block as the load cavity.

Cesium carbonate and potassium were used to generate the cesium beam used in this experiment. The potassium was forced into thin-walled stainless steel tubing of 0.125-inch diameter, which was crimped at the ends in order to prevent oxidation of the potassium during the time required for loading. One end of the tubing was uncrimped immediately before placing the potassium in the source. Whenever the source load was to be changed, the source was left in the apparatus, but it was washed thoroughly with water, alcohol, and acetone. A normal source temperature was approximately 80° C.

41

During all of the runs it was found that the amount of beam drops to an unusable level after about 200 hours of continuous running time. The reason for this failure is not known. In all cases the source was loaded with approximately 0.1 gram of cesium carbonate and 0.1 gram of potassium. This amount of load material should produce a usable beam for periods longer than 6 months because of the material-saving qualities of the crinkly-foil source-tube assembly (34). With a slightly different source design, but the same load materials, Yates and Haun (34) obtained a beam that lasted for 6 weeks — even then the source showed no sign of giving out. Daly and Holloway (7) use glass ampoules containing approximately one gram of pure cesium in their crinkly-foil sources. These ampoules are broken under vacuum and produce beams for periods longer than 1000 hours. Zacharias and Weiss (37) also report success with pure cesium ampoules.

c. Deflecting Magnets

One of the deflecting magnets is shown in a cut away drawing in Fig. 25. The deflecting magnets consist of Armco iron pole faces with Alnico V permanent magnets. The return yoke, which is also the enclosing box, consists of 0.5-inch-thick cold-rolled steel in the shape of two U's that are bolted together at the tops of the legs. The ends of the magnet boxes are covered with 0.125-inch-thick cold-rolled steel sheets with holes through which the beams can pass. Straightedges that help to define the beam are mounted on these end plates.

The important parameters of the deflecting magnets (see Fig. 26) are:

Length of deflecting region, 3.50 inches

2a, 0.500 inch

Gap width (tip of convex to valley of concave), 0.250 inch

The magnets are magnetized by discharging momentarily several submarine storage batteries through a permanent 10-turn copper winding that goes around the Alnico bars. This copper winding is composed of $1/2 \times 1/4$-inch copper bar.

The field in the gap was measured at the convex pole face with a germanium Hall-effect probe built by J. H. Holloway (11). The fields of the two magnets were adjusted so that they were equal within 1 per cent during the original magnetization process by making comparisons with this probe.

The stray field from the magnets was measured 2 inches from the ends of the magnet boxes with a flip-coil and galvanometer. With the end plates installed, the stray field is approximately one gauss. Without the end plates, this value rises to approximately 100 gauss.

The wide gaps and short lengths were chosen so that low-velocity atoms with their necessarily large deflections could be used. (See Appendix III.)

Since it was felt that the desired magnetic fields could be calculated with sufficient accuracy and could then be set within this accuracy during the magnetization process, no provision was made to alter these fields while the apparatus is under vacuum.
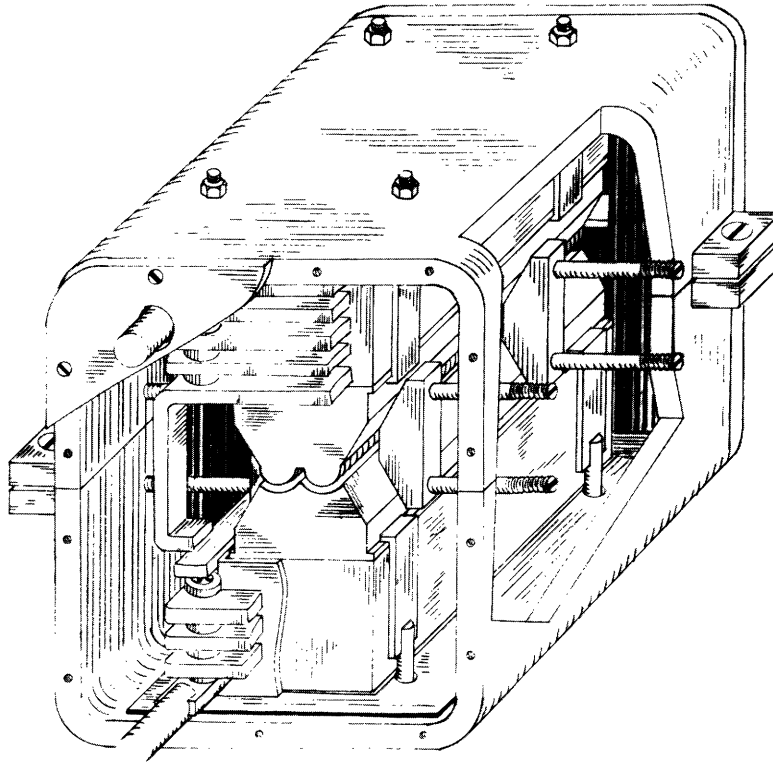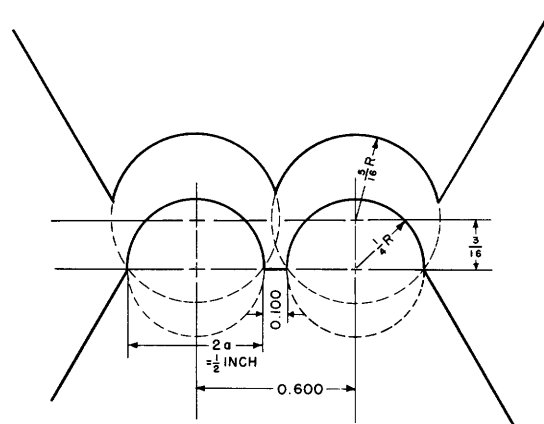
Fig. 25. Deflecting magnet.

Fig. 26. Deflecting-magnet gap dimensions.

d. Detector

The detector consists of a surface-ionization detector, a magnetic-momentum spectrometer, an electrostatic-energy spectrometer, and an electron multiplier. The output of the electron multiplier is fed directly into the dc amplifier of a Sanborn recorder. (See Fig. 27.)

The surface ionization detector (12) is a tungsten ribbon $0.001 \times 0.040 \times 2.5$ inches mounted in a rectangular box. The face of this box is insulated from the rest of the box so that an accelerating voltage can be applied between the plane containing the detector ribbon and the opposite side of the box. The detector ribbon is heated to approximately 800° C by running an alternating current of approximately 1.7 amp through it. This current is obtained from a transformer-variac combination.

The mass spectrometer is a 30° wedge with a 0.125-inch gap between the pole faces. The atom beam passes through this gap, strikes the hot ribbon, and is re-emitted as a beam of ions which is deflected in the mass spectrometer. The mass-spectrometer magnet consists of the Armco iron pole faces, Alnico V permanent magnets (1-inch diameter, each approximately 2 inches long), and a cylindrical cold-rolled-steel return yoke that encloses the pole faces and the Alnico magnets. The return yoke is 3/16 inch thick. The field in the 0.125-inch gap is 3.4×10^3 gauss, as measured with a germanium Hall-effect probe.

After being deflected by the mass spectrometer, the ion beam passes between the top plates of a circular, cylindrical, electrostatic condenser. This electrostatic deflection rotates the plane of the ion beam "ribbon" approximately 30° so that the ions hit the first plate of the electron multiplier at the spot that gives the greatest gain. The voltages applied to the deflector plates and to the detector ribbon are obtained from a regulated power supply. Potentiometers are provided so that the value of the accelerating voltage (applied to the detector ribbon) can be varied. The ratio of the deflecting voltage to this accelerating voltage can be set with another potentiometer. For cesium, V_{accel} is approximately 100 volts and the ratio V_{defl}/V_{accel} is about 1/3.

The electron multiplier is an eleven-stage multiplier of the Allen type (1). The plates are of beryllium-copper and the voltage divider chain (mounted directly on the multiplier) consists of 10-megohm 0.5-watt carbon resistors. The entire multiplier is mounted inside a cold-rolled-steel box that can be removed from the apparatus by loosening two bolts. A hole 0.5-inch in diameter in the wall of the box is placed so that the ion beam can reach the first plate of the multiplier. The high voltage required to operate this multiplier was obtained from a Spellman rf supply that was run off a regulated 300-volt supply. Gains as high as 10^7 have been obtained with 280 volts per stage. A more typical value is 10^6.

Before the multiplier was first assembled, the plates were polished with fine jeweler's rouge and stored under acetone. The multiplier was fired by induction heating under vacuum to a temperature of approximately 500° C (dull red, not visible in a well-lighted room) for about 20 minutes. When it was necessary to refire the multiplier, it
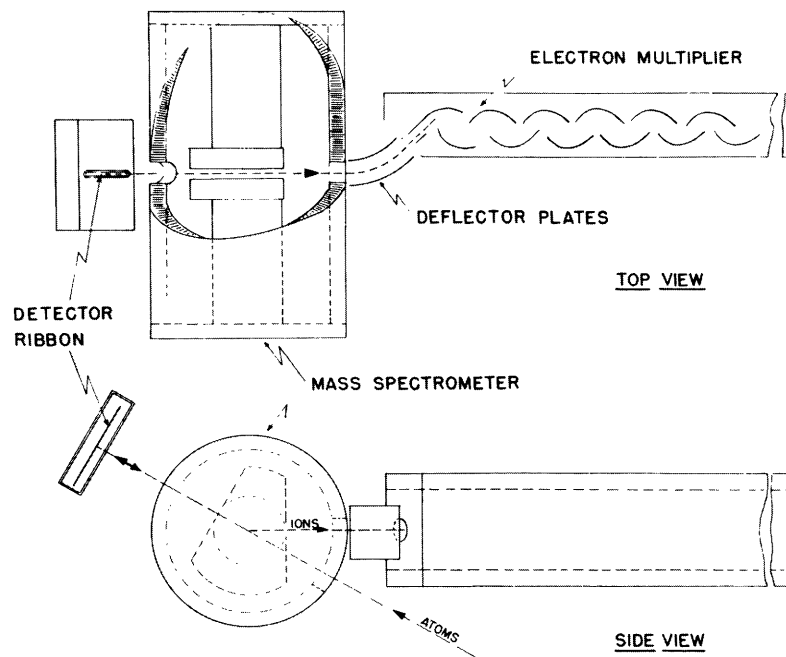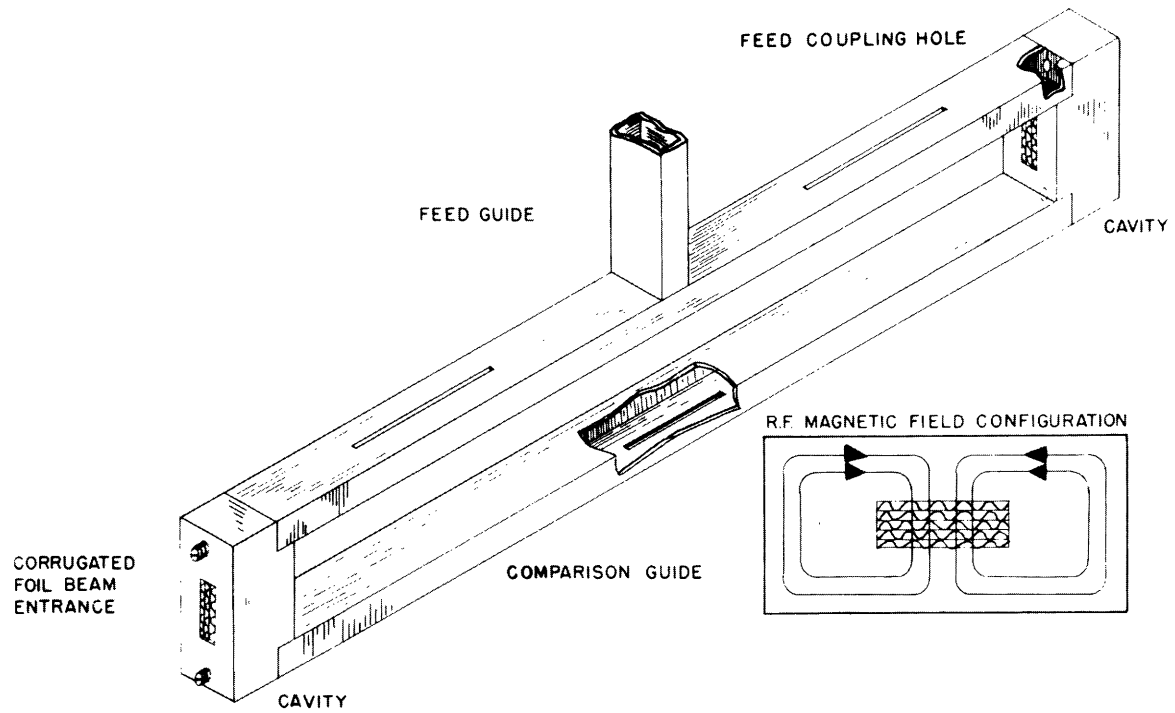
Fig. 27. Detector.

Fig. 28. High-frequency transition cavities.

45

was not taken apart but was merely degreased with acetone and alcohol and heated as described above.

As can be seen in Fig. 27, the direction of the deflection in the mass spectrometer is in the plane of the beam so that high resolution would not be expected. The main purpose of the spectrometer is to eliminate potassium background caused by potassium ions that leave the detector ribbon. The electrostatic deflector plates were used so that the ion beam could be directed toward that portion of the first electron-multiplier plate that gives highest gain.

The output of the electron multiplier is fed directly into the amplifier of the Sanborn recorder (input impedance, 5 megohms) or into the Sanborn preamplifier (input impedance can be chosen as high as 100 megohms). These amplifiers are very stable and have sensitivities of 1.5 cm/50 mv and 1.5 cm/5 mv, respectively. Provision was made to vary the time constant at the input of the Sanborn amplifiers with an external circuit.

e. High-Frequency Transition Cavities

The microwave transition cavities and feed system used in this apparatus are similar to the system designed by Yates for the feasibility-study test model (34). The cavities and feed system are shown in Fig. 28.

The two cavities are rectangular, each being equivalent to a piece of rectangular waveguide two half-wavelengths long. (The cavity dimensions are $0.500 \times 0.688 \times 3.000$ inches.) The walls of the cavities are copper. The beam enters and leaves each cavity through a pair of $1 \times 1/4$-inch slots cut in the 3/8-inch-thick walls. These slots are filled with corrugated copper foil with corrugations approximately 0.020 inch deep. (See Appendix IV.) This foil allows the beam to pass through with a loss of approximately 30 per cent in each slot, while it acts as an array of waveguides operating beyond cutoff to keep the microwave field inside the cavity. This guarantees that the transitions take place in the rectangular space defined by the cavity dimensions.

The microwave radiation is fed to the cavities through a piece of rectangular X-band waveguide that is coupled magnetically to the cavities at its ends through holes in the cavity walls. The microwave radiation enters this waveguide through a Tee at the center point which is fed from outside the vacuum can. The cavities were matched to the feed guide by filing the coupling holes to give minimum standing-wave ratio in the feed guide. The feed guide is 30.75 inches long.

The relative phase of the rf fields in the two cavities can be adjusted with two tuning screws that are inserted in each cavity. A probe is inserted in the middle of the comparison guide and the cavities are tuned to give minimum power at this point.

During one of the Stark-effect runs asymmetrical resonance curves were obtained in the "up" beam, while almost asymmetrical curves were obtained in the "down" beam. Upon opening the apparatus it was found that some oxalic acid had fallen on the upper rf cavity as the upper source was being given a special cleaning. The resulting
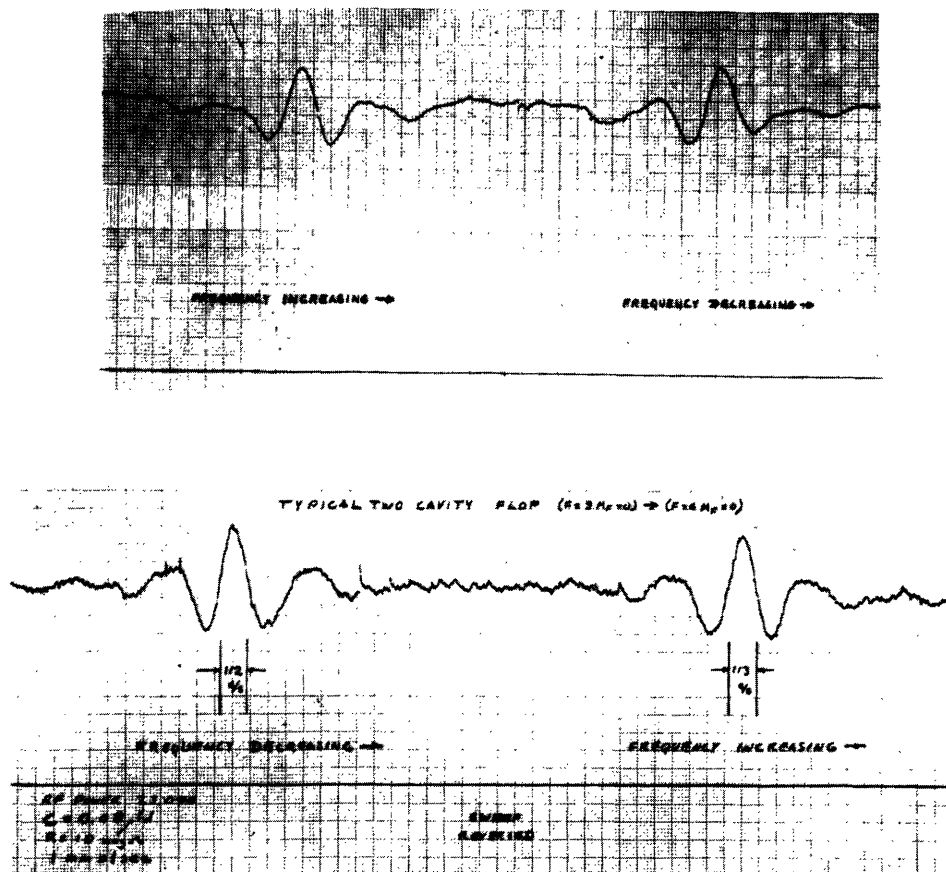
Fig. 29. Typical resonance curves (optimum rf power),
before and after washing out cavities.

blue-green deposit was assumed to be copper-oxalate and the cavities were washed out
thoroughly with ammonium hydroxide, dilute nitric acid, water, acetone, and alcohol.
The rf system was not altered in any other way. When Ramsey resonances were next
observed, the resonance curves in the "up" beam were found to be more nearly asym-
metrical. We therefore conclude that it is possible to introduce in one of the cavities
a localized loss that is so large that the relative phase of the oscillating fields that
effect the beam will depend upon which part of the cavities the beam passes through.
Figure 29 shows the resonance curves obtained in the "up" beam before and after
cleaning out the cavities.

f. Helmholtz Coils

The magnetic field at the two transition cavities can be varied with a set of orthog-
onal Helmholtz pairs. The current for these coils is obtained from a pair of 6-volt
storage batteries.

g. Low-Frequency Transition Coils

As auxiliary equipment two low-frequency coils are installed near the high-frequency
transition cavities. These coils are used to induce the $(F=4, m_F=-4) \leftrightarrow (F=4, m_F=-3)$

47

transition. These coils are useful in the initial warm-up of the source, since the presence of the beam can be detected only by the appearance of atoms that undergo radio-frequency transitions. (This is because offset geometry is used.) A General Radio Type 805A signal generator is used for the low-frequency-transition exciting source — approximately 1.4 volts at the 75-ohm output being necessary to produce transitions at 300 kc.

h. Line-Up Wires and Jigs

Since the locations of the beam-tube components cannot be changed while the apparatus is under vacuum, a fairly precise line-up procedure was necessary. In order to provide a reference plane for the initial line-up of the apparatus, a steel wire was stretched along one edge of each of the two U-channels. The position of one end of each of these wires could be adjusted. With the apparatus in a horizontal position, these wires were lined up with respect to a number of vertical wires. This established a reference plane from which all of the other line-up measurements could be made by using a jig and micrometer.

The line-up dimensions are shown in Fig. 4, and the calculations leading to this choice of parameters are outlined in Appendix II.

2. FREQUENCY GENERATION

a. General

The preliminary observations of the Stark effect on cesium[133] hyperfine structure were made with the use of a microwave triode oscillator developed by Yates (33, 23) as the exciting source for the transitions. However, the power output from this oscillator was just barely sufficient, and the rate of sweep of the output frequency was not as linear as one might wish. Therefore, an X-band version of an S-band phase-stabilized klystron system of the type developed by C. L. Searle and D. D. McRae (29, 17) was built.

This frequency source (see Fig. 30) consists of an X-band klystron (operating at 9192.6 mc), the output of which is mixed in a balanced microwave mixer with a weak 9192.8-mc signal derived from a pair of crystal oscillators. The resulting 200-kc difference signal is amplified by a wideband high-gain i-f amplifier and fed into a phase detector where it is compared with a standard signal from a stable General Radio signal generator. The output of the phase detector is inserted in series with the repeller supply voltage for the klystron, and in this way the klystron is phase-locked to the crystal harmonics and to the 200-kc signal generator.

This frequency source was found to be extremely reliable. It has the advantage that the output frequency, when the klystron is locked, is as stable as the signals to which the klystron is locked, and if the klystron is not locked, then (assuming that the servo loop is in good working order) the output frequency will be far enough from 9192.6 mc so that no error will result.
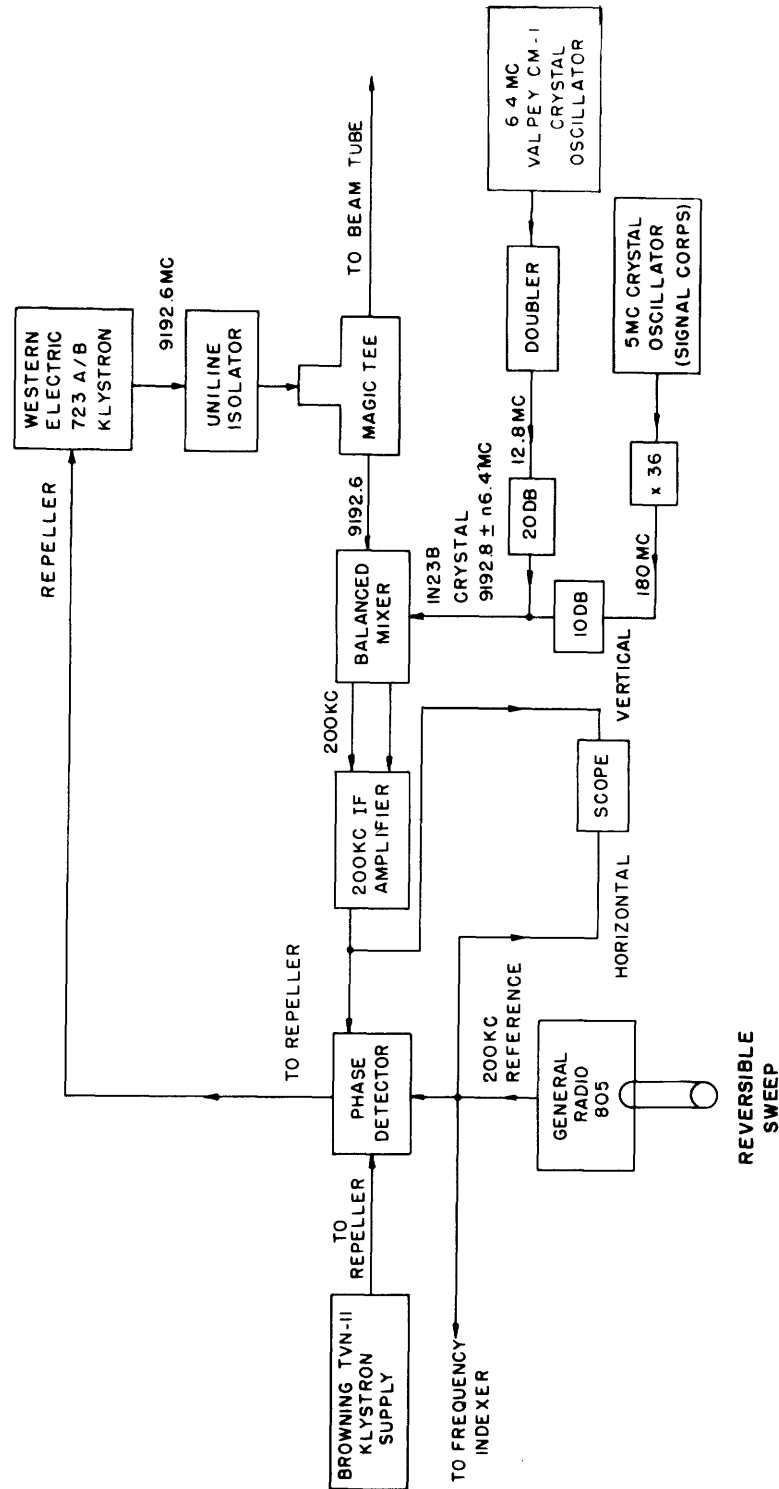
Fig. 30.   Crystal-stabilized klystron frequency source.

b. Locking-Frequency Synthesis

1. General discussion. The locking frequency at 9192.8 mc was obtained by generating 9180 mc/sec (the 51st harmonic of 180 mc/sec) from 180 mc/sec in a 1N23B crystal and mixing this in the same crystal with a 12.8 mc signal. Both of these signals were obtained from crystal oscillators and vacuum-tube multipliers.

2. Five-megacycle oscillator and multiplier chain. The 180-mc signal was obtained by multiplying from 5-mc in a multiplier chain constructed by D. S. Edmonds.

During the preliminary runs with the Yates oscillator, two crystal oscillators were tried and found unsatisfactory as 5-mc sources.

i. A 5-mc oscillator with a Valpey crystal enclosed in a thermostatically controlled heated box was used first. This oscillator was unsatisfactory because stray capacitative effects caused the output frequency of the oscillator to change by 3 parts in 10^8 every time the thermostat opened or closed. This effect was eliminated by removing the thermostat; but then, because of rapid thermal drifts, the crystal was not sufficiently stable.

ii. A Western Electric 100-kc crystal oscillator which, with its associated thermal control, is stable to a few parts in 10^{10} was used next, but it was found to be unsatisfactory because in the multiplication by 50 from 100 kc to 5 mc too much noise was introduced for the resulting signal to be useful for stable measurements at X-band. The "noise" in the output was equivalent to random-frequency fluctuations of 1 part in 10^8.

To overcome these difficulties, a 5-mc crystal oscillator, with an 80° C AT cut Signal Corps crystal in a Miller circuit, was constructed. This circuit was mounted on a massive brass plate which was placed on top of a 5-gallon can filled with water. The whole apparatus was enclosed in a large thermally insulated box and was heated with a 200-watt light bulb fed from a variac. The temperature of the oscillator was kept at 80° C by reading once a day a thermometer placed on the brass plate and readjusting the light bulb power if necessary. Since the thermal time constant for this arrangement was of the order of hours, excellent short-term stability could be obtained. This was sufficient for the experiment because only frequency differences were to be measured. A typical value for the amount of drift in any 24-hour period was approximately 1° C.

The multiplier output at 180 mc (approximately 2 watts) was attenuated with a 10-db pad and then fed directly into the 1N23 crystal.

iii. 6.4-mc oscillator and doubler. The 12.8-mc signal was obtained by doubling the 6.4 mc output of a crystal oscillator.

A 6.4 mc Valpey CM-1 crystal was used in a Miller oscillator circuit. This signal was doubled in a 6AQ5, followed by a 6CL6 cathode follower. The resulting 12.8-mc output (approximately 1 watt) was attenuated with a 20-db pad and fed into the 1N23 mixer-multiplier crystal.

iv. Frequency sweep. The 200-kc standard signal was obtained from a General Radio Type 805A signal generator. Since the klystron is phase-locked, its frequency will vary exactly the same number of cycles per second as the Type 805 if the Type 805 frequency is changed. During the Stark-effect measurements, the frequency of the Type 805 signal generator was varied by moving the tuning knob by a belt drive connected to a synchronous electric motor. The direction of sweep could be reversed manually by pressing a reversing button. The rate of sweep used for most of the measurements was approximately 15 cycles/sec^2.

It is interesting to remark that the phase-stabilized klystron will remain in lock for variations of the Type 805 frequency as great as 100-kc from the optimum value of 200 kc.

c. Waveguide Circuitry and the Klystron

The klystron used to provide the 9192.6-mc signal was a Western Electric Type 723A/B (2K25). This klystron and all of the associated microwave circuitry were not shielded from the environment in any way, either thermally or electrically, nor was any attempt made to shock-mount the apparatus. All of the power for the klystron (including the ac filament heater) was obtained from a Browning TVN-11 klystron power supply.

This klystron was connected to the load through a microwave isolator (Uniline, made by Cascade Research Corporation) that provides approximately 10 db of reverse attenuation. The klystron output was divided into two parts in a Magic Tee, one half going to the mixer for the phase-lock system, and the other half going to the rf cavities in the atomic-beam vacuum tube. In this section we discuss only that part of the microwave circuit that is necessary for the phase-stabilization operation.

The 9192.6-mc signal from the klystron is fed into the H-arm of an X-band Magic-Tee mixer (16, 18). The 9192.8-mc signal derived from the two crystal oscillators in a 1N23 crystal mounted in a tunable crystal mount (16) enters the Magic Tee through the E-arm. Tunable crystal mounts with 1N23B crystals are mounted on the other two arms of the Magic Tee (these arms will be referred to as the "side arms"). The 200-kc frequency difference is detected in these crystals and fed into the balanced input of the i-f strip.

Best results are obtained if considerable care is taken in balancing the Magic Tee. If this is not done, two difficulties arise:

1. The signals at the two side-arm crystals from the klystron are not adequately balanced so that noise from the klystron is amplified in the i-f strip and fed back to the repeller through the phase detector. This results in self-sustained oscillations of the servo loop.

2. Enough 9192.6-mc power leaks into the E-arm to give cross modulation between the 9192.6 mc, the 180 mc and its harmonics, and the 12.8 mc and its harmonics. Since very little power is needed for the i-f strip to produce a large enough signal at

51

the phase detector for lock, there will be a large number of spurious lock-in points that are closely spaced in the frequency domain — with the net result that the lock of the klystron to the "correct" (i.e., 9192.8 mc) power will be very poor.

d. The I-F Amplifier and the Phase Detector

The i-f strip and phase detector are printed circuits provided by C. L. Searle (29, 17). The i-f amplifier is a wideband (approximately 100-kc passband), high-gain (approximately 100 db) amplifier operating at approximately 200 kc. A regulated 200-volt power supply was used for this circuit. The filaments were heated by alternating current.

The phase detector is fairly straightforward except for the addition of a lag network in the output of the circuit. This lag network is necessary to introduce a loss at frequencies that are well off the center frequency (200 kc) in order to prevent the occurrence of loop oscillations as a result of phase shifts in the i-f strip. The tuning of this network is fairly critical, but the correct adjustment can easily be determined by trial and error when the phase-stabilized klystron is first put into operation. Both the lag network and the Magic-Tee balance needed no further adjustment during a four-month period after the original tune-up.

e. Monitoring the Phase-Lock and Frequency

The lock of the 200-kc difference between the klystron and the standard (9192.8 mc) signal to the 200-kc signal from the Type 805 signal generator was monitored continuously throughout all of the measurements by observing the elliptical pattern produced by feeding the two 200-kc signals into the X- and Y-amplifiers of an oscilloscope.

Since the 200-kc difference signal is phase-locked to the Type 805 signal-generator output, it makes no difference which signal is used for the frequency measurement. Since only one crystal oscillator and multiplying chain was available, it was not possible to check the frequencies of the crystal oscillators continuously within the high precision required for this experiment. Therefore the signal at 9192.8 mc was assumed to be stable within one part in 10^9 (or better) during the time required for a measurement. This stability assumption was verified from time to time by turning off the frequency sweep while on the side of the central peak of a resonance curve (see sec. 4.5).

3. FREQUENCY MEASUREMENT — THE FREQUENCY INDEXER

The frequency difference (f_d) between the klystron-output frequency (f_k = 9192.6 mc) and the standard frequency (f_s = 9192.8 mc) was compared with the 60-cps frequency in the (Cambridge, Massachusetts) electric lines in order to monitor the frequency of the klystron. This comparison was carried out in a circuit that generates a marker pulse (which can be applied to one pen of the Sanborn recorder) every time the frequency changes by 60 cps. This circuit (see Fig. 31), which we shall call the "frequency indexer," was suggested by J. G. King.

The frequency f_d is fed into a Type 6BE6 mixer where it is heterodyned with a stable signal f_a. In the Stark-effect experiment f_a was obtained from a General Radio Model 1001A signal generator. The audio-frequency difference f_b, between f_a and f_d, is fed into another 6BE6 mixer, where it is combined with the output from a 60-cps multivibrator, which is synchronized with the 60-cps (Cambridge, Massachusetts) electric lines. Since all of the 60-cps harmonics are present in the multivibrator output, the beat f_c between the multivibrator output and the unknown f_b will contain only multiples of 60 cps every time f_b is a multiple of 60 cps. The beat f_c is passed through a notching filter network which strongly attenuates 0 ± 2 cps, 60 ± 2 cps, 120 ± 2 cps, 180 ± 2 cps, and 240 ± 2 cps. Combined with this filter is a lowpass filter that attenuates frequencies above 30 cps. The output of this filter is then amplified and rectified. The rectified voltage is used to control a relay. When the relay closes, a mark appears on the lower margin of the Sanborn recorder chart.

The operation of the circuit can be described as follows: When f_c is less than 30 30 cps, but larger than 2 cps, the signal can pass through the notching filter and reach the relay control tube. The bias of this control tube is adjusted so that the relay is open for this condition. But when f_c is less than 2 cps, no signal passes through the notching filter and the bias of the relay control tube changes, so that the relay closes — with the result that a mark appears on the recorder chart.

The lowpass filter with cutoff at 30 cps is necessary because there is the possibility that the beat between f_b and one of the harmonics in the multivibrator output may give a very strong signal at n60 cps, where n is greater than 4. If the cutoff at 30 cps were not present, there might not be a marker pulse, even though the frequency f_b would be a multiple of 60 cps. The cutoff at 30 cps also eliminates one of the two sidebands of the beat between f_b and n60. The filters at 60, 120, 180, and 240 cps are necessary because it is difficult to make a perfect high-frequency cutoff.

The net result is that, as the klystron frequency is varied with the Type 805 signal generator, a frequency "index" mark appears on the Sanborn recorder every time the
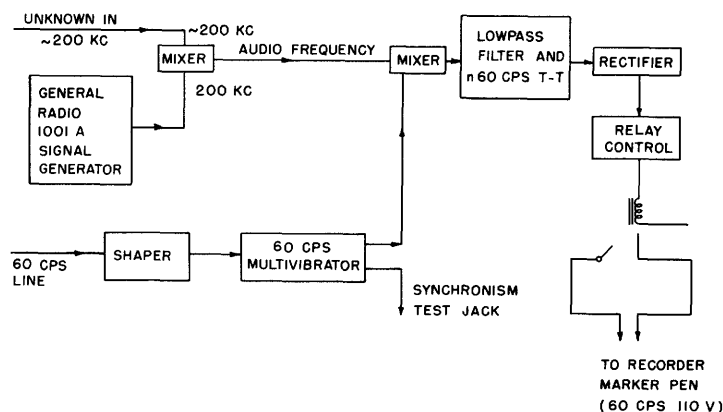

Fig. 31. Frequency indexer.

frequency has changed by 60 cps. (It is assumed that the crystal oscillators and the Type 1001A signal generator are stable during the time required for a measurement.)

For an input f_b of approximately 10 volts, the frequency indexer has been found to produce markers reliably, every 60 cycles over a range of 190 markers; that is, the frequency indexer will operate up to the 85th harmonic of the 60-cps fundamental.

A synchronism test jack was provided on the multivibrator so that the lock of the multivibrator to the 60 cps (Cambridge) electric lines could be checked with an oscilloscope. The multivibrator frequency was adjusted by varying the B^+ supply voltage to the frequency indexer.

As a check on the frequency during the intervals between markers, the audio beat frequency f_b was monitored continuously by a loud-speaker. Sudden jumps in the 805 output could be detected in this way. These rarely occurring jumps were usually caused by looseness of the automatic-sweep drive belt and were never larger than 20 cps.

If the unknown input signal is too small, a spurious marker may appear midway between two 60-cps markers. These spurious markers occur because the 30 cps high-frequency cutoff acts as a 30-cps notch for weak signals. These markers can be identified as spurious by noting whether or not the audible-frequency monitor indicated a jump at this point.

CORRUGATED-FOIL SOURCES

Since the solid angle that the detector subtends at the source is small, only a small fraction of all the atoms leaving the source will be useful in an atomic-beam apparatus. This waste of beam material is one of the factors that could limit continuous-use life-time of an atomic-beam frequency standard. For this reason, a "well-collimated" source beam-exit-tube assembly has been developed from which a considerable saving in beam material has resulted, unaccompanied by a prohibitive reduction in the amount of useful beam. These well-collimated sources were used in both the feasibility-test model and in the apparatus described in this report.

In this appendix the theoretical basis for the material-saving characteristics of the sources, the methods of construction and use, and the results of experiments for testing the material-saving characteristics of the ovens, will be discussed.

Suppose that a single, circular, cylindrical tube of length L and cross-section area A connects the interior of the source with the main vacuum system. Let $\vec{n}$ be the nor-mal to the partition between the source and the main system. Let ϕ be the angle between $\vec{n}$ and a straight line connecting the centers of the main system and the source tube with some point P in the main system. And let dN be the number of atoms per second that leave the source through the tube and reach a small solid angle $d\omega$ located at point P.

Then, for $L^2/A = 0$, it follows from solid-angle considerations that

$$\frac{dN}{d\omega} = \left(\frac{dN}{d\omega}\right)_{max} \cos \phi$$

where $\left(\frac{dN}{d\omega}\right)_{max}$ is the value of the flux directly along the axis of the source tube. The total number N of atoms per second leaving the source is just the integral taken over the half-unit sphere on the high-vacuum side of the partition chamber:

$$N = \int\int \frac{dN}{d\omega} \sin \phi \, d\phi \, d\theta$$

for $L^2/A = 0$, this integration gives

$$N = \pi \left(\frac{dN}{d\omega}\right)_{max}$$

The solid angle d subtended by the detector in an atomic-beam apparatus is small, so that the number N_b $\left(\doteq \left(\frac{dN}{d\omega}\right)_{max} d\Omega\right)$ of atoms that makes up the useful beam is small in comparison with N.

A considerable gain in the ratio N_b/N can be obtained without any reduction in N_o by making L^2/A much greater than unity and keeping A constant. When this is done,

$\left(\dfrac{dN}{d\omega}\right)_{max}$ remains the same as for $L^2/A = 0$, while N is reduced by a factor of approximately $(A/L^2)^{1/2}$. (See refs. 13, 5, 31, 6.) Therefore, to conserve source material, we make L^2/A as large as possible for the source tube.

However, a further complication arises because of the possibility of collisions between the beam atoms while they are still inside the source tube. Let λ be the mean free path for beam atoms at the pressure inside the tube. Then, if $\lambda < L$, the plane $L - \lambda$ from the high vacuum and of the source end of the source tube will act as a diffuse source of atoms. Therefore the effective length of the tube will be only $L < \lambda$, instead of L. If $\lambda > L$, then the effective length of the tube will be just the geometrical length L. Now, $\lambda = K/P$, where K is a constant dependent only on the gases in the source, and P is the vapor pressure of the gas in the exit tube at the source operating temperature T. However, $\left(\dfrac{dN}{d\omega}\right)_{max}$ is proportional to a positive power of P. Consequently, L must be made small so that the source can be operated at sufficiently high pressure to give a sufficiently large value of $\left(\dfrac{dN}{d\omega}\right)_{max}$.

In order to satisfy both of these requirements simultaneously, L^2/A must be made large and L small; hence A must also be made small. Since the forward intensity is proportional to the cross-section area of the slit, the single tube must be replaced by a large number, N_s, of tubes, each of which has its axis parallel to the axes of the others. The walls separating these tubes must be as thin as possible.

Let A_{total} be the total cross-section area of the tube assembly — including the area blacked out by the walls separating the tubes from each other. The effective area of the tube assembly is $N_s A$, where A is now the cross-section area of each tube (all tubes are assumed to be identical). The value of $\left(\dfrac{dN}{d\omega}\right)_{max} d\Omega$ for the tube assembly will be $A N_s/A_{total}$ multiplied by the value of $\left(\dfrac{dN}{d\omega}\right)_{max} d\Omega$ for a single tube of cross-section area, A_{total}. (The quantity $A N_s/A_{total}$ will be referred to hereafter as f.) Since the thickness of the walls between tubes is finite, f will always be less than unity for N_s greater than one. The obvious requirement that f be as nearly equal to unity as possible, together with the fact that the strength of materials places a lower limit on the thickness of the walls between tubes, sets a practical upper limit on the value of L^2/A.

A practical value of L was found to be 0.5 inch. Tubes could then be made with a cross-section area of 8×10^{-6} inch^2. (For ease of manufacturing, the cross section of each tube is made roughly triangular rather than circular. This introduces only minor changes in the arguments given above.)

The source-tube assemblies are constructed as follows: Nickel foil, 1 mil thick, is run between two interlocking bronze rolls in the faces of which axial grooves have been milled. The resulting corrugated sheet has grooves 0.002 inch deep with "peak-to-peak" groove widths of approximately 0.010 inch. The corrugated sheet is cut to the desired length and stacked in layers between flat sheets of the nickel foil (i. e., a corrugated sheet, a flat sheet, a corrugated sheet, and so on).
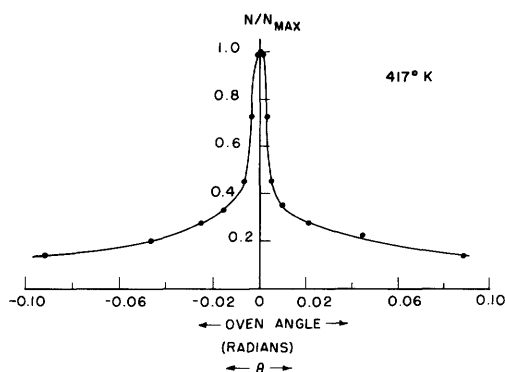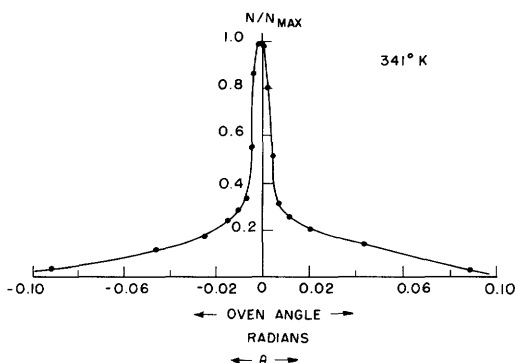
N/N_MAX
417° K
OVEN ANGLE →
(RADIANS)
← θ →

Fig. 32. Corrugated-foil source tube assem-
bly beam distribution.

N/N_MAX
341° K
OVEN ANGLE →
RADIANS
← θ →

The material-saving factors of these source assemblies were tested by rotating a source about an axis that passes through the high-vacuum end of the source-tube assembly, and observing the beam with a fixed detector. The source-tube assembly used for the observations that are plotted in Fig. 32 was 1 inch X 0.040 inch. The value of f for this assembly was approximately 0.3. The detector used to measure the atom flux was a 2 inch by 0.040 inch tungsten ribbon placed approximately 2 feet from the source.

The ratio of the amount of material leaving the assembly per unit time to the amount of material that would leave an infinitely short slit of the same effective area is given, approximately, by

$$g = \frac{N_{total} \text{ for the infinitely short slit}}{N_{total} \text{ for the tube assembly}} = \frac{\pi \left(\frac{dN}{d\omega}\right)_{max}}{2\pi \int_0^{2\pi} \left(\frac{dN}{d\omega}\right)_{observed} \sin\phi \, d\phi}$$

This is only an approximation, since the tubes are not figures of revolution. The value of g for the assembly was approximately 150 at 70° C.

Since there is actually a distribution of mean free paths between collisions (as a result of the Maxwellian velocity distribution), some of the beam atoms will always suffer collisions in the source tubes. The slower atoms will predominate in this group.

For the atoms that suffer collisions, the effective length of the tube will be less than L. The fraction of atoms suffering collisions within the tube will increase with increasing source temperature (i.e., with increasing beam-material vapor pressure). The portions of the angular distribution curves in Fig. 32, for ϕ greater than approximately 0.04 radian, are made up, predominantly, of these scattered atoms. It can be seen from the two curves plotted in Fig. 32 that the parts of the curves for ϕ greater than 0.04 radian increase rapidly as the source temperature is increased.

Experimental curves for tubes with a smaller L^2/A ratio than for the tubes described in this report will be found in reference 8.

$$I(m) \text{ FOR THE VELOCITY DISTRIBUTION } \frac{dN}{d\left(\frac{v}{a}\right)} = \begin{cases} 0 & 0.6 \geq \frac{v}{a} \geq 2.3 \\ -1.95 + 3.25\frac{v}{a} & 0.6 \leq \frac{v}{a} \leq 1.0 \\ 2.30 - 1.00\frac{v}{a} & 1.0 \leq \frac{v}{a} \leq 2.3 \end{cases}$$

m	I(m)	m	I(m)
0	1.1050		
.5	1.0037	10.5	.1184
1.0	.7244	11.0	.0989
1.5	.3334	11.5	.0802
2.0	−.0812	12.0	.0605
2.5	−.4409	12.5	.0304
3.0	−.6639	13.0	.0127
3.5	−.7493	13.5	−.0176
4.0	−.7015	14.0	−.0481
4.5	−.5606	14.5	−.0743
5.0	−.3721	15.0	−.0931
5.5	−.1916	15.5	−.1023
6.0	−.0425	16.0	−.1014
6.5	.0738	16.5	−.0973
7.0	.1462	17.0	−.0771
7.5	.1788	17.5	−.0590
8.0	.1911	18.0	−.0295
8.5	.1883	18.5	−.0193
9.0	.1761	19.0	−.0038
9.5	.1585	19.5	.0102
10.0	.1385	20.0	.0248

APPENDIX VI

SAMPLE DATA SHEETS

In Figs. 33, 34, 35, and 36 typical recordings of the shift of the $(4, 0) \longleftrightarrow (3, 0)$ transition frequency caused by an electric field are shown. The values of the relative rf power and the voltage applied to the Stark electrodes have been varied in choosing these curves. Other curves have been given in preceding sections of this report.
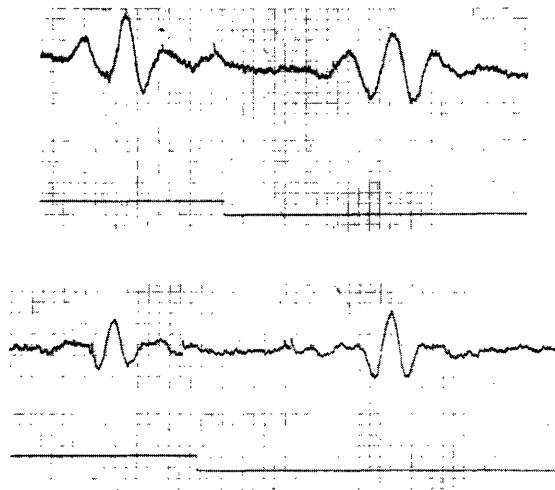

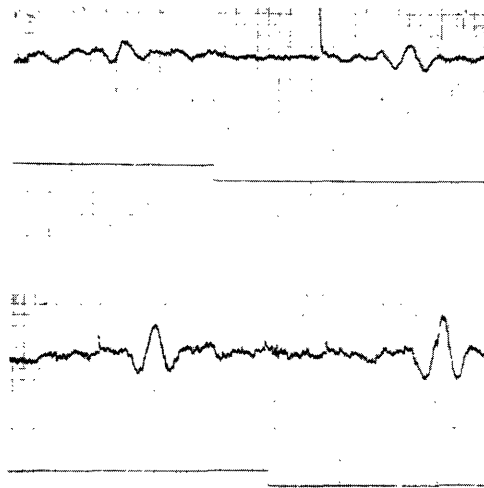Fig. 33. Typical data recordings. Run No. 1, +3 db power, 19.92 ± .04 kv; -3 db power, 20.03 ± .04 kv.

Fig. 34. Typical data recordings. Run No. 2, -9 db power, 20.06 ± .04 kv; Run No. 1, -6 db power, 19.92 ± .04 kv.

60
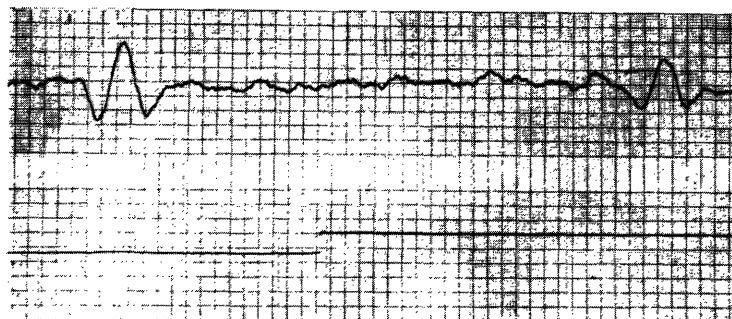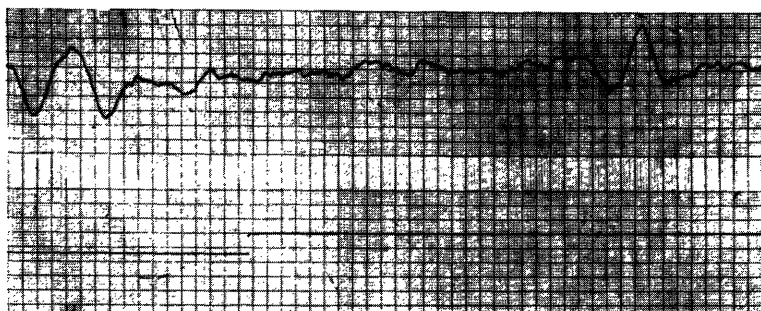
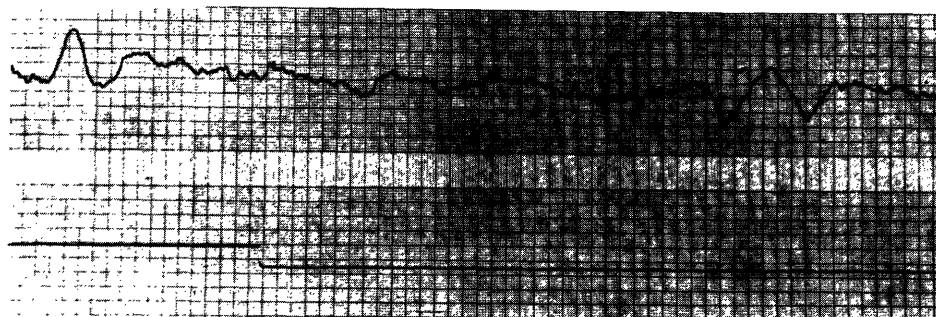Fig. 35. Typical data recordings. Run No. 4, +2 db power, 24.42 ± .04 kv; -2 db power, 24.46 ± .04 kv.

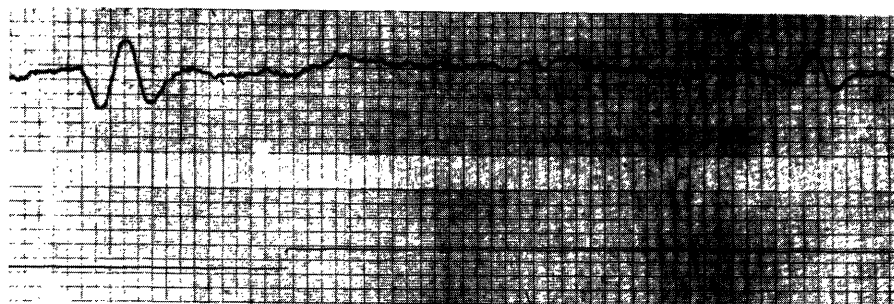Fig. 36. Typical data recordings. Run No. 4, -2 db power, 27.24 ± .14 kv; +4 db power, 27.29 ± .14 kv.

61

Acknowledgment

References

1. J. S. Allen, Proc. IRE **38**, 346 (1950); Rev. Sci. Instr. **18**, 739 (1947).

2. G. Breit and I. I. Rabi, Phys. Rev. **38**, 2082 (1931).

3. E. U. Condon and G. H. Shortley, The Theory of Atomic Spectra (Cambridge University Press, London, 1953), p. 422.

4. Ibid., p. 34.

5. P. Clausing, Z. Physik **66**, 471 (1930).

6. P. Clausing, Physica **9**, 70 (1929).

7. R. T. Daly and J. H. Holloway, private communication; paper presented at Brookhaven National Laboratory Molecular Beam Conference, October 1956.

8. L. Davis, Jr., The hyperfine structure of Na^{22}, Technical Report 88, Research Laboratory of Electronics, M.I.T., Dec. 1, 1948.

9. L. Essen and J. V. L. Parry, Nature **176**, 280 (1955).

10. I. Estermann, Revs. Modern Phys. **18**, 300 (1946).

11. J. H. Holloway, Ph.D. Thesis, Department of Physics, M.I.T., 1956.

12. J. B. M. Kellogg and S. Millman, Revs. Modern Phys. **18**, 323 (1946).

13. J. G. King and J. R. Zacharias, Some new applications and techniques of molecular beams, Advances in Electronics and Electron Physics, Vol. VIII (Academic Press, New York, 1956),

14. U. E. Kruse and N. F. Ramsay, Jr., J. Math. Phys. **30**, 40 (1951).

15. P. M. Morse and H. Feshbach, Methods of Theoretical Physics (McGraw-Hill Book Company, Inc., New York, 1953), p. 1244.

16. C. G. Montgomery, Technique of Microwave Measurements, Radiation Laboratory Series Vol. 11 (McGraw-Hill Book Company, Inc., New York, 1947).

17. D. D. McRae, S.M. Thesis, Department of Electrical Engineering, M.I.T., 1955.

18. R. V. Pound, Microwave Mixers, Radiation Laboratory Series Vol. 16 (McGraw-Hill Book Company, Inc., New York, 1948), Chap. 6.

19. N. F. Ramsey, Molecular Beams (Oxford University Press, London, 1956), see especially Chap. 3.

20. N. F. Ramsey, Nuclear Moments (John Wiley and Sons, Inc., New York, 1953), Chap. 2.

21. I. I. Rabi, J. R. Zacharias, S. Millman, and P. Kusch, Phys. Rev. **55**, 526 (1939).

22. N. F. Ramsay, Phys. Rev. **78**, 695 (1950).

23. R. H. Rearwin, S.M. Thesis, Department of Electrical Engineering, M.I.T., 1954.

24. C. H. Schwartz, private communication, 1955.

25. R. Scheffers and J. Stark, Physik. Z. **35**, 625 (1934).

26. C. H. Schwartz, private communication, 1956.

27. C. H. Schwartz, Phys. Rev. **97**, 380 (1955).

28. K. F. Smith, Molecular Beams (Methuen and Company, Ltd., London, 1955).

29. C. L. Searle and D. D. McRae, Stabilization of klystrons by phase locking to low-frequency quartz crystal oscillators, Quarterly Progress Report, Research Laboratory of Electronics, M.I.T., April 15, 1956, p. 37.

30. J. C. Slater, Quantum Theory of Matter (McGraw-Hill Book Company, Inc., New York, 1951), pp. 388 ff.

31. M. von Smoluchowski, Ann. Physik 33, 1559 (1910).

32. A. G. Worthing and J. Geffner, Treatment of Experimental Data (John Wiley and Sons, Inc., New York, 1943), p. 189.

33. J. G. Yates, Stable-frequency microwave oscillator, Quarterly Progress Report, Research Laboratory of Electronics, M.I.T., Jan. 15, 1954, p. 59.

34. J. R. Zacharias and J. G. Yates, Cesium clock, Quarterly Progress Report, Research Laboratory of Electronics, M.I.T., Oct. 15, 1954, p. 30; J. R. Zacharias and R. D. Haun, Jr., Well-collimated atomic beam ovens, Ibid., p. 34.

35. J. R. Zacharias, J. G. Yates, and R. D. Haun, Jr., Proc. IRE 43, 364 (1955).

36. J. R. Zacharias, Phys. Rev. 61, 270 (1942).

37. J. R. Zacharias and R. Weiss, private communication,